## Title

Multidisciplinary Investigations of Chalcogen-based Semiconductor Materials: Structural Heterogeneity, Strain Analysis, and In-Situ Mechanical Testing



## Author

Sari, Bengisu

## Publication Date

2023

Peer reviewed|Thesis/dissertation

# Multidisciplinary Investigations of Chalcogen-based Semiconductor Materials: Structural Heterogeneity, Strain Analysis, and In-Situ Mechanical Testing

By

Bengisu Sari

A dissertation submitted in partial satisfaction of the

requirements for the degree of

Doctor of Philosophy

in

Engineering- Materials Science & Engineering

in the

Graduate Division

of the

University of California, Berkeley

Committee in charge:

Professor Mary C. Scott, Chair
Professor Andrew M, Minor
Professor Ali Javey

Fall 2023

Multidisciplinary Investigations of Chalcogen-based Semiconductor Materials: Structural Heterogeneity, Strain Analysis, and In-Situ Mechanical Testing

Abstract

Multidisciplinary Investigations of Chalcogen-based Semiconductor Materials: Structural Heterogeneity, Strain Analysis, and In-Situ Mechanical Testing

by

Bengisu Sari

Doctor of Philosophy in Engineering- Materials Science & Engineering

University of California, Berkeley

Professor Mary C. Scott, Chair

Thin films with semiconducting properties can be successfully engineered from chalcogen-based materials, specifically those containing selenium (Se), or/and tellurium (Te). They are vital subjects of study in both their elemental states and various compounds due to their distinct anisotropic properties. These elements play essential roles in compounds like tellurides and selenides, which are crucial in semiconductors, photovoltaic devices, and electronics. However,the quick crystallization tendencies observed in amorphous $Te_xSe_1 - x$ thin films restrict their applicability. It is essential to gain insight into the short- and medium-range structural organization of the amorphous state and comprehend the underlying physics driving film crystallization. Therefore, in the second chapter of the thesis, we provide comprehensive research on the short- to medium-range ordering in amorphous $Te_xSe_1 - x$ thin films through a combination of experimental studies and atomic simulations. This study marked the first instance in which we employed fluctuation electron microscopy (FEM) and Density Functional Theory (DFT) calculations to gain insights into these structural variations across a wide range of compositions, including pure Te. Within the chain network structure, we have identified at least two distinct populations that closely resemble the intrachain distances of Se-Se and Te-Te. In the case of the binary alloy with $x$ greater than 0.61 in $Te_xSe_1 - x$, we observe an increase in Te-Te-like populations, implying the potential formation of Te fragments.

To leverage the anisotropic properties of tellurium, in recent study, the oriented growth of ultra-thin Te layers on a $WSe_2$ substrate is achieved by using a technique called physical vapor deposition (PVD). In this configuration, the atomic chains of Te align with the armchair directions of the substrate, leading to the formation of a moiré superlattice. This superlattice consists of micrometer-scale Te flakes positioned on the continuous $WSe_2$ film. Here, we explore the exact orientation relationships and moiré lattices by combining electron microscopy with image simulations. We also assess the strain evolution and defects in Te-$WSe_2$ heterostructures with the help of scanning nanodiffraction analysis, shedding light on the complexities of strain transfer and its impact on

material properties.

In the final chapter of the thesis, we introduce a hybrid approach aimed at addressing challenges in sample preparation for in-situ mechanical testing. It involves depositing samples on flexible, electron-transparent substrates, attaching them to macroscopic copper sheets, and mirroring techniques used in the nanomaterials and thin-film community. With the help of this technique, we were able to study the mechanical responses of sputtered gold (Au) and transition metal dichalcogenides (TMDC), specifically $WS_2$. This method not only streamlines sample preparation but also expands our ability to investigate the mechanical properties of materials at the nanoscale.

to Dogancan Sari and my grandmother

# Contents

# List of Figures

# List of Tables

# Acknowledgments

I extend my deepest gratitude to Prof. Mary C. Scott for her unwavering support, kindness, and exemplary leadership. As a woman in the scientific community, she has not only guided me academically but has also been a source of profound inspiration. Her commitment to fostering diversity within our lab and her efforts in organizing social activities have created an inclusive environment that I am proud to be a part of. I am immensely grateful to have been one of the initial four graduate students in our group, witnessing firsthand the remarkable growth and evolution of our research cohort under Prof. Scott's guidance. Prof. Scott's role as a role model for everyone in our academic community has been invaluable, and her dedication to nurturing talent and encouraging individual growth has left an indelible mark on my academic journey.

I extend my sincerest gratitude to Prof. Ali Javey, Prof. Daryl Chrzan and Prof Andrew Minor for their invaluable assistance during the most challenging aspects of my studies. Their guidance illuminated pathways to navigate through complex problems, providing essential insights and perspectives. I am immensely proud to have had the opportunity to collaborate with them, and their expertise has significantly enriched my academic journey. Being a part of Prof. Javey's lab provided me with a remarkable opportunity to immerse myself in the vibrant materials development community. Collaborating with the lab not only expanded my academic horizons but also allowed me to actively contribute to this dynamic field.

My heartfelt gratitude goes to Dr. Colin Ophus for being an indispensable guide in the computational aspects of my studies. His patient mentorship and dedication in sharing invaluable insights have been pivotal throughout my PhD journey. Dr. Ophus not only imparted crucial knowledge but also generously devoted his time to provide guidance whenever I faced challenges in my projects. His support and willingness to share ideas have been instrumental in shaping the trajectory of my research.

I wish to express my deepest appreciation to Rohan Dhall, not only for his invaluable assistance and guidance in academic pursuits but also for generously sharing his wealth of career and life experiences. Dr Dhall's mentorship has been a guiding light during moments of uncertainty, offering insights that transcended academia. His kindness, unwavering positivity, and brilliance as a scientist made our collaboration a cherished experience. The opportunity to work alongside such a remarkable individual will be dearly missed. I extend my heartfelt thanks to Karen Bustillo and John Turner for their unwavering support in facilitating access to electron microscopes and for their exceptional kindness and positivity throughout my research journey.

I wish to express my sincere appreciation to my collaborators, Steven Zeltmann, Chunsong Zhao, and Medha Dandu, for their invaluable expertise and unwavering support in addressing challenging problems. I would also like to extend my gratitude to my close friends and collaborators, Humberto Batiz Guerrero and Ana Isabel, for their continuous support and camaraderie throughout our collaborative endeavors.

I extend my heartfelt appreciation to all members of the Scott group for fostering an environment that is not only supportive and collaborative but also immensely enjoyable. I would like to express my profound gratitude to two outstanding individuals within the Scott group, Alex Bruefach and Ellis Kennedy, who have not only been invaluable colleagues but also my closest friends.

I want to dedicate this thesis to my mom and dad. Their unwavering dedication to raising me to be independent and resilient has been the cornerstone of my journey. Their constant presence, endless love, and unwavering support have been the bedrock upon which I've built my aspirations and achievements. This thesis stands as a tribute to their guidance and love, for they have been my pillars in every step I've taken.

Lastly, I want to thank my spouse, Dogancan Sari. Your unwavering support, belief in me, and sharing our dreams mean the world. Your encouragement has been my strength. The unity and warmth we share have created a beautiful extended family, for which I am immensely thankful. Finally, our new family member Gofret, our dog, for bringing cherish to our lives.

# Chapter 1

# Introduction

## 1.1 Motivation

A chalcogen refers to an element belonging to the chalcogen group of the periodic table, which includes oxygen (O), sulfur (S), selenium (Se), tellurium (Te), and polonium (Po). Although they share similar oxidation states and are grouped under the same family, their chemical and physical properties vary. Specifically, oxygen, sulfur, and selenium are classified as nonmetals, while tellurium falls under the category of metalloids. The classification of polonium as a metal or a metalloid remains uncertain. Chalcogens, when they form compounds by combining with other elements or compounds, find applications in a wide range of fields. These applications include photovoltaics, photocatalysis, sensors, fuel cells, and batteries, showcasing their versatile role in modern technology and research [1]. In the context of this research, our primary emphasis was placed on investigating the properties and behavior of tellurium and selenium chalcogens, as well as transition metal dichalcogenides (TMDCs).

### Chalcogenide Glasses

Telluride glasses, also known as chalcogenide glasses, are a class of amorphous materials composed primarily of tellurium (Te) combined with elements such as sulfur (S), selenium (Se), and other chalcogens. These glasses are particularly interesting for their unique properties and applications in optoelectronic and non-volatile memory devices. One of the key characteristics of telluride glasses is their ability to switch between amorphous (glassy) and crystalline phases by heating or electrical stimulation resulting in changes in reflectivity, resistivity, and optical transmission in the mid-infrared region. These properties enable a range of applications in photonics, electronics, and sensing technologies[2, 3, 4]. Understanding and developing phase change materials (PCMs) indeed involves a deep understanding of their amorphous structure and finding ways to create more stable amorphous phases. Although there has been an ongoing research on the reasons why some amorphous alloys are more stable than the others such as amorphous Zr–Cu–Ni–Al alloys, it is claimed that the short- to medium- range orders affect the crystallization temperature and so the stability of the amorphous state when the structures of the precipitating phase and the short-range

order in amorphous are not similar [5]. Therefore, it is critical to reveal the local orders in PCMs with the help of advanced characterization techniques.

## Moiré Structures, Strain, and Defects in Tellurium Films

Throughout history, thin films of tellurium have found applications in electronics, such as thin film transistors, variable resistors, and sensors [6]. This is due to their notable characteristics, including high hole mobility and significant photoconductivity[7]. In recent times, there has been a resurgence of interest in Te, after it's orientation-dependent optical/electronic properties have emerged due to the anisotropic nature of the tellurium crystal. It has been shown that the room-temperature mobility of tellurium reaches approximately 707 $cm^2V^{-1}s^{-1}$ in Te crystals with a thickness of merely 16 nanometers, particularly when oriented along the high-mobility axis [8]. In our previous study, we systematically demonstrated the controlled deposition of Te crystalline films on transition metal dichalcogenides (TMD), such as $WSe_2$ , $WS_2$ , $MoSe_2$ , and $MoS_2$ [9]. In the case of $WSe_2$, we note that the c-axis of tellurium aligns with the armchair direction of the substrates.In addition, we unveil the the emergence of moiré lattices resulting from the interaction between these substrate and the film. The moiré structure exhibits spatial variations, giving rise to fascinating properties like superconductivity, topological conducting channels, and advanced optoelectronic behaviors, as previously documented [10]. Nonetheless, capturing these microscopic variations through imaging poses a non-trivial challenge. While the potential to tailor the optoelectronic characteristics of a heterostructure by stacking multiple layers is appealing, it's crucial to acknowledge that the transfer of strain between distinct van der Waals layers can result in significant alterations in a material's electronic, quantum transport, and photonic properties, especially as the structural complexity increases, as documented in prior studies [11, 12, 13].

## Advanced Strain Platform for In-Situ Mechanical Testing of Thin Films in TEM

The field of materials science has long investigated the mechanical properties of materials, particularly how crystalline systems respond to mechanical stress. These responses are tied to elastic stiffness constants like bulk and shear modulus, providing insights into the nature of chemical bonding and symmetry elements within crystals[14]. However, excessive strain can lead to crystal defects such as dislocations and twins, which influence a material's response to stress and may cause phase transitions or fracture [14, 15]. The transmission electron microscope (TEM) is unique in its ability to directly visualize the changes in the atomic structure of a material, including the generation of defects in a crystal lattice under load, and hence, in-situ mechanical deformation has been a subject of interest for material scientists since the early 1960s [15]. Nonetheless, the main problem in this research is sample preparation. Existing methods often rely on rigid straining platforms or complex systems involving focused ion beam (FIB) preparation. For thin film community , the fabrication of macroscopic dog-bone structures for tensile testing was infeasible. To address these challenges, tensile tests were conducted on thin films deposited on flexible substrates, such

as polyimide (e.g., poly-imide cited in [16] or Polydimethylsiloxane (PDMS) cited in [17]. However, both of these systems encounter difficulties in sample preparation. Hence, there's a demand for more flexible and simpler methods of sample preparation to study the mechanical behavior of materials within TEMs.

## 1.2 Experimental Methods

### Four-Dimensional Scanning Transmission Electron Microscopy (4DSTEM)

The materials science tetrahedron emphasizes the five interdependent, distinct aspects of materials science, with vertices representing processing, structure, properties, performance, and characterization at its center. As depicted in the tetrahedron, the ability to understand and control matter can only be achieved through advanced characterization tools. Imaging, measuring, modeling, and manipulating matter can be accomplished with the help of Transmission Electron Microscopy (TEM) [18]. TEM stands out as one of the most powerful and versatile characterization tools used in nanoscale science, engineering, and technology.

Thanks to advances in detector systems and the high degree of flexibility provided by electromagnetic lenses, various modes have emerged. One of the most popular techniques is Scanning Transmission Electron Microscopy (STEM) due to its ability to perform multiple types of measurements simultaneously. In STEM, a high-energy beam is focused onto a sample surface and rastered across the sample [19]. In traditional STEM, at every position of the beam, the electrons are scattered through a detector and populate each pixel to form a two-dimensional image. In fact, different detector geometries lead to varying image contrast based on their distinct electron scattering processes [20]. The recent invention of pixelated detectors enables researchers to capture a two-dimensional (2D) image of the diffracted electron beam at each probe position. This technique is known as 4DSTEM and paves the way for collecting high-resolution real and reciprocal space information simultaneously, leading to spatially resolved maps of phases[21], grain orientations[22], and lattice strain [23]. Moreover, for non-crystalline samples, local ordering can be detected using probe sizes similar to the short- or medium-range orders [24] with the assistance of 4DSTEM. This allows for various measurements to be performed from a single 4D-STEM dataset. By employing the 4DSTEM technique, we have not only revealed the atomic ordering in amorphous Te$x$Se$1-x$ alloys but also resolved moiré structures related to strain relaxation mechanisms in the Te/$WSe_2$ system.

### Radial Distribution Function

Defining the amorphous structure is crucial for understanding the order or "structure" in amorphous materials. Although the pioneering work in defining the amorphous structure was carried out by J.D. Bernal, who revealed the cavities within the amorphous structure by filling containers packed with ball bearings with paint and then studying the contact points from the residual dried

paint, the most common method involves distribution functions obtained through experimental or computational studies [25].

The radial distribution function (RDF) illustrates how the density of surrounding matter changes as a function of distance from a point. In this technique, the relative abundance of interatomic distances around an arbitrarily chosen atom is measured. The diffracted mean intensity, arising from independently scattering atoms, deviates as the local density around this arbitrarily chosen atom alters. To deduce the structural parameters from diffraction data, we should begin with the scattered intensity given by the Debye formula and average it for all directions. Equation 1.1 shows the scattered intensity:

$$I(q) = Nf^2(q) + 4\pi Nf^2(q) \int^{\infty} 0[g(r) - \rho 0]\frac{r}{q} - \sin(qr)dr \tag{1.1}$$

where $Nf^2(q)$ is the mean intensity term originating from the scattering of atoms, and the other part depicts the deviation from this mean intensity if the local density at distance $r$ deviates from the mean density $\rho_0$. In fact, if the amorphous structure lacks structural heterogeneities, the mean intensity curve would be a parabolic curve without any deviations. To extract the radial distribution function, $g(r)$ or $4\pi Nf^2(q)(g(r) - \rho_0)$, we define the structure factor or reduced intensity function term:

$$\phi(q) = \left[\frac{I(q) - Nf^2(q)}{Nf^2(q)}\right] q \tag{1.2}$$

Structure factors can be retrieved by removing and dividing the single atom scattering factors from the mean intensity. Single atom scattering factors are calculated using the parameterization as described by Lobato [26]. It is also possible to subtract a polynomial function from the mean intensity to obtain the reduced intensity function. The radial distribution function is then retrieved by applying a discrete sine transform to the calculated structure factor (Equation 1.3):

$$G(r) = \int^{\infty} 0\phi(q)\sin(qr)dq = 4\pi Nf^2(q)[(g(r) - \rho 0)] \tag{1.3}$$

where $G(r)$ is the reduced RDF, and $g(r)$ is the traditional RDF.

This approach has been widely used to unravel the short-range ordering in amorphous structure with the help of electron diffraction due to the larger scattering cross-section for electrons [27, 28, 29, 30], the flexibility of imaging the area of interest, and allowing smaller volumes of material to be investigated [31]. Despite its advantages over other techniques, electron diffraction is susceptible to multiple scattering. While it does not affect the interatomic distances in RDF results, it does affect the determination of coordination numbers.

## Fluctuation Electron Microscopy

In highly disordered materials, short-range configurational order is established over the scale of bond distances that can extend to several coordination shells. Information regarding bond lengths, coordination numbers, interaction potentials can be probed by extended X-ray absorption fine

structure (EXAFS) [32], X-ray photoelectron spectroscopy (XPS) [33] , nuclear magnetic resonance (NMR) [34], and electron microscopy [28]. One of the common techniques discussed in Section 1.2 is the radial distribution function.

In the first couple of coordination shells, any technique using partial pair correlation functions is adequate. However, when attempting to measure the orderings beyond the short-range orders, the pair correlation functions are not a unique description of the atomic structure since they represent an average over polar as well as azimuthal angles. In disordered materials, the atomic structure beyond the short-range ordering (1-3 nm) is called medium-range orders, and higher-order correlation functions are required to reveal the possible structures [24, 35].

Fluctuation Electron Microscopy (FEM) is a quantitative technique to unravel the ordering beyond the short-range order by using TEM [36]. FEM uses a statistical approach to measure nanometer-scaled orders from diffraction data and is reported to be sensitive to three- and four-body correlation functions. It is based on the idea that if a beam size is comparable to the sizes of the medium-range orders, scattered electrons constructively interfere, resulting in larger diffracted intensity. To measure the local changes in the diffraction data, we compute the variance of the intensity distributions:

$$V(k,Q) = \frac{\langle I^2(r,k,Q)\rangle - \langle I(r,k,Q)\rangle}{(\langle I(r,k,Q)\rangle)^2} \tag{1.4}$$

where $I(r,k,Q)$ is the spatially averaged diffracted intensity as a function of the sample's position [24]. The reason for using $\langle I^2\rangle$ instead of $\langle I\rangle$ is because $\langle I^2\rangle$ is sensitive to three- and four-body correlations.

FEM measurements can be performed by using dark-field imaging in conventional microscopes [36] or nanobeam diffraction patterns collected using the raster-scanned probe [35, 24, 37]. In this work, we will focus on the latter method due to its efficient use of electron dosage and time. Additionally, we are not limited by the physical nature of the objective aperture.

Although FEM is an effective technique, several sources of experimental artifacts, such as sample thickness, roughness, a distribution of voids, and oxidation, can seriously affect the magnitude of the variance peaks and lead to misinterpretations [38]. Therefore, care must be taken to collect high-quality and reproducible data sets.

## 1.3 Thesis Overview and Contents

In Chapter 2, our research combined experimental studies with atomic simulations to conduct a comprehensive study uncovering the short- to medium-range ordering in amorphous Te-Se thin films. We prepared Te$x$Se$1-x$ thin films with varying compositions ($x = 0.22, 0.61, 0.70, 0.90,$ and 1) through thermal evaporation. Electron diffraction enabled the investigation of short-range orders (SROs) and medium-range orders (MROs) within these non-crystalline TeSe thin films. Moreover, measurements of radial distribution functions (RDFs) showcased alterations in bond lengths associated with compositional changes. Utilizing fluctuation electron microscopy (FEM) from scanning nanodiffraction data revealed the presence of two distinct MRO populations upon

introducing selenium (Se) into the amorphous Te thin films. Collaborators performed density functional theory (DFT) calculations for six compositions, yielding RDFs closely mirroring experimental observations, suggesting varying bond character's role in evolving MRO populations with increasing Se content.

Chapter 3 elucidated the orientation relationship between WSe2 and Te, along with the moiré effect, employing scanning nanodiffraction and image simulations. This revealed a moiré superlattice comprising micrometer-sized Te flakes atop continuous WSe2 films. Differential phase contrast (CoM-DPC) techniques enabled visualizing the moiré lattices for the first time in this material system. Understanding strain evolution during thin film growth and post-growth behavior in Te-WSe2 heterostructures is crucial for broadening their applications. Scanning nanodiffraction helped assess strain levels and identify defects within Te, revealing non-uniform strain in both Te and WSe2 films. Additionally, significant rotation and associated dislocations were observed in specific areas of the Te film.

In Chapter 4, we introduced an approach to overcome challenges in preparing samples for in-situ mechanical tests in TEM. This method involves placing samples on a flexible substrate allowing electron passage and bonding them to large copper sheets using Crystalbond. These copper sheets serve as stress concentrators and specimen carriers, compatible with the Gatan 654 straining holder. This sample preparation process closely resembles conventional TEM methods, enabling thin films to be applied through spin coating, sputter coating, or wet transfer onto the flexible substrate. We applied this method to both gold-sputtered thin films and TMDC WS2 flakes.

# Chapter 2

# Structural Heterogeneity in Non-Crystalline $Te_x$ $Se_{1-x}$ Thin Films

Rapid crystallization behavior of amorphous $Te_xSe_{1-x}$ thin films limits the use of these alloys as coatings and in optoelectronic devices. Understanding the short- and medium-range ordering of the amorphous structure and the fundamental physics governing the crystallization of the films is crucial. Although the lack of long range crystalline order restricts the characterization of the amorphous films, electron microscopy offers a way to extract information about the nanoscale ordering.

This chapter is devoted to reveal the local ordering of amorphous $Te_xSe_{1-x}$ thin films with $x = 0.22, 0.61, 0.70, 0.90, 1$ by using radial distribution function (RDF) and fluctuation electron microscopy (FEM) analysis. RDF results show that the nearest-neighbor distances of selenium (Se) and tellurium (Te) in their crystalline structure are preserved and their bond lengths increase with the addition of Te. Density functional theory (DFT) calculations predict structures with interatomic distances similar to those measured experimentally. Additionally, fluctuations in atomic coordination are analyzed. Medium range order (MRO) analysis obtained from FEM and DFT calculations suggests that there are at least two populations within the chain network structure which are close to the Se-Se and Te-Te intrachain distances. For the binary alloy with $x > 0.61$, $Te_xSe_{1-x}$ , Te-Te like populations increases and Te fragments might form, suggesting that the glass forming ability decreases rapidly.This chapter is reproduced from [39], with the permission of AIP Publishing.

## 2.1 Introduction

Telluride glasses have recently been the subject of renewed interest for applications in optoelectronic and non-volatile memory devices due to their ability to switch between glassy and crystalline phases, which also changes their reflectivity, resistivity, and optical transmission in the mid-infrared [2, 3, 4]. Although reversible crystallization driven by thermal excitations is desirable for switching devices, telluride glasses for optical applications must be resistant to crystallization to

avoid scattering losses. To utilize Te-based glasses for both of these applications, it is crucial to understand the crystallization kinetics of the glasses to reliably control crystallization and stabilize amorphous phases.

Lacking long-range crystalline order, it is atomic ordering on shorter scales—termed short-range order (SRO) or medium-range order (MRO), depending on the length scale of the ordering—that influences the properties of amorphous materials. For example, it has recently been shown that SRO in the amorphous matrix affects the glass forming ability and the crystallization in metallic glasses [27, 40]. Studies have also shown that the crystallization temperature is reduced when the short and medium range ordering in the melt are similar to those found in the precipitating crystalline phase [5]. While these previous studies have focused on metallic glasses [41, 42, 35, 43] and amorphous silicon($a$-Si) [44, 24, 31], this work will characterize the binary $Te_xSe_{1-x}$ system. This material serves as a model system to study phase-change materials (PCM), since it undergoes reversible phase switching through melting, melt-quenching into an amorphous phase, and crystallization [45, 46]. Past studies indicate that Se and Te consist of chain-like clusters in their amorphous states, with atomic structures that resemble their crystalline phases [47, 48]. The main difference between two crystal structures is stemmed from the interchain bond strenght. Interchain bonding in selenium is mainly van der Waals (vdW) bonds, while Te chains are bonded relatively stronger with metallic and van-der Waals bonds.

The distribution of the Se and Te atoms within the chain-clusters have been studied in the past using X-ray and [49, 50] neutron [29] diffraction, nuclear magnetic resonance (NMR) [46, 3], and Raman spectroscopy [51]. In theory, the Te and Se atoms can be randomly distributed, organized in a homogeneous arrangement, or organized with a chemical ordering that reflects a preference for heteropolar bonds. Although no consensus has been reached, the majority of studies claim that Te and Se atoms are randomly distributed into chains with a slight preference of the heteropolar bonds. M. Majid & J. Purans also added that intrachain chemical ordering increases with Te content in the glass for up to $x = 0.4$ at% Te [50]. Although crystalline Se and Te alloys form a continuous series of solid solutions because of their similar crystalline structures [52], the characterization of amorphous Te is more challenging because of its rapid crystallization at room temperature. Therefore, experimental results of $Te_xSe_{1-x}$ alloys with higher Te concentrations, including pure amorphous Te, are still not widely reported in the literature.

Detecting nanoscale ordering in amorphous solids with the help of neutrons and X-rays is experimentally challenging due to the low scattering cross section, resulting in a small scattered signal to be used for the study of nanovolumes. The use of characterization techniques reliant on electron-material interactions increases the scattering cross section compared to x-ray methods and improves spatial resolution in RDF measurements [53].

In this work, a systematic study of changes in SRO and MRO in $Te_xSe_{1-x}$ amorphous as a function of composition is presented. $Te_xSe_{1-x}$ thin films with $x = 0.22, 0.61, 0.70, 0.90, 1$ are prepared by thermal evaporation. The SROs and MROs in non-crystalline $Se_xTe_{1-x}$ thin films are investigated using electron diffraction. RDF measurements show alterations in bond lengths with changes in composition. FEM measurements indicate two populations of MRO that arise as Se is added. DFT calculations of the amorphous structures are used to help in interpreting experimental measurements. DFT calculations conducted for six different compositions produce RDFs similar

to those observed experimentally, and suggest that bond character differences are the origin of the changing MRO populations with increasing Se content.

## 2.2 Experimental details

### Thermal Evaporation of Amorphous Thin Films

We synthesized $Te_xSe_{1-x}$ thin films with compositions of $x = 0.22, 0.61, 0.70, 0.90, 1$ using an Edwards Coating System (E306A thermal evaporator system).The base pressure was approximately $1.6 \times 10^{-6}$ mbar. When the pressure reached $2 \times 10^{-6}$ mbar, we decreased the substrate temperature down to $-80\,^{\circ}$C using a liquid nitrogen flow. We used NORCADA 10 nm amorphous $Si_3N_4$ grid as substrates and kept their temperature at $-80\,^{\circ}$C during the deposition to prevent the crystallization. With the exception of pure Te, we allow the substrate temperature to return to room temperature after evaporation. Since pure Te is fully crystallized at room temperatures, we quenched the sample in liquid nitrogen as soon as the deposition was completed.

The thickness of the films were monitored during the deposition, and were also confirmed using electron energy loss spectroscopy on an FEI Tecnai operated at 200 kV with a C2 aperture of 150 µm, a camera length of 42 mm, and an entrance aperture of 2.5 mm. We used the zero-loss peak to calculate the film thickness within the Digital Micrograph software. The Fourier log deconvolution indicated a $t/\lambda$ value of 0.185 corresponding to a thickness of $22 \pm 2$nm for this composition of Te-Se. We determined the compositions by energy-dispersive x-ray spectroscopy (EDS) maps collected from 3 different regions of each film.

### Data Collection and Analysis

For RDF analysis, we collected parallel beam diffraction patterns for each composition on an FEI TitanX, operated at 200 keV. Diffraction acquisition parameters were 160 mm and 0.1 s exposure times. Pixel sizes were calibrated with a calibration gold sample with known lattice parameter values for both RDF and FEM analysis. We used custom python scripts in the py4DSTEM package to obtain the RDF, (g(r)), from the diffraction patterns [20]. The beam stop was removed from the diffraction patterns and elliptical distortion corrected to obtain the polar mean of the data. The intensity profile was normalized by the single atom scattering factors which were calculated using the compositions of Te and Se in the sample according to the parameterization published in Ref. [26] to retrieve the structure factors. Smaller camera lengths were used for the RDF measurement to include the high scattering angles, which helps to fit the single scattering factors to the intensity profiles. It is crucial to provide a masking function to the structure factor to remove the incomplete tails in the structure factors. Finally, we calculated the radial distribution function g(r) through a discrete sine transform of the structure factors. We determined the peak positions in RDF by measuring the positions that correspond to a maximum.

FEM patterns were collected on the TitanX, operated at 200 keV with convergence angle 0.51 mrad, a probe diameter of 2.2 nm, and a camera length of 245 mm. To prevent crystallization

and beam damage, and to avoid oversampling, we chose 0.3 s exposure times and 5 nm step sizes. For all compositions, to prevent the crystallization driven by electron beam, we collected data from the regions far away from the places where beam alignment was carried out. Examples of parallel beam diffraction patterns for amorphous Te before and after the scanning nanodiffraction experiments are shown in Supplemental Material (SM) Figure 2.5, indicating no beam-induced crystallization. Since the calculation of the variance is a statistical approach, for each composition over 2500 scanning nanodiffraction images were collected in one scan. We collected 4 scans for each of the compositions. For FEM data analysis, the removal of the ellipticity and determination of the differences in variance as a function of the spatial frequency were performed by a custom MATLAB script. We determined the peak locations by fitting individual Gaussian functions to each peak location as shown in the SM Figure 2.6. Standard errors in variance plots were calculated from the root mean squared deviation for each composition.

### Computational procedure

DFT computations were conducted using the Vienna Ab initio Simulation Package [54, 55, 56] version 5.4.4. The projected-augmented-wave method was used [57], and the exchange-correlation energy was modeled using Perdew-Burke-Ernzerhof functional [58]. Starting from a $4 \times 4 \times 4$ Te supercell (a total of 192 atoms), we created $Se_xTe_{1-x}$ initial structures with $x = 0$, 0.20, 0.40, 0.50, 0.60, 80 by randomly replacing Te atoms with Se atoms. Using a 600 eV cutoff energy for the plane-wave basis set, a single k-point at $\Gamma$, and convergence criteria of $10^{-4}$ eV for the electronic self-consistent cycle, we created five $Se_xTe_{1-x}$ alloys for each composition as follows: First, classical molecular dynamics simulations based on DFT computed forces and sampling the NPT ensemble using the Parrinello-Rahman method [59] were performed. The time step was chosen to be 1 fs, and six initial structures, one for each composition, were heated up to 1000 K in 200 steps and held at that temperature for at least 14000 steps. Then, the atomic species in the heated structure were randomly swapped to create 4 new configurations. Finally, we ran 5 arrangements for 1000 steps at 1000 K before minimizing their configurational energy with a conjugate gradient algorithm. For all of the simulated systems, the root mean square displacement of the atoms was at least 7 Å.

## 2.3 Results and Discussion

Figure.2.1 shows the RDF analysis for the whole composition range of the non-crystalline Te-Se system extracted from electron diffraction and DFT calculations. A vertical offset was applied to the curves to distinguish them easily. There are two distinct peaks in each RDF curve at R(Å) $<$ 3.0 and 3.5$<$ R(Å) $<$4.5. These two well-defined peaks were also observed in RDF calculations obtained by our simulations. The first and second peak positions are plotted in Fig. 2.2 (a) and (b) respectively. The position of the RDF peaks obtained from both the experiment and the simulations exhibit the same trend: the first peak in the data from the highest Se concentration film is at 2.34 Å and increasing the Te content results in longer distances between the nearest neighbors.

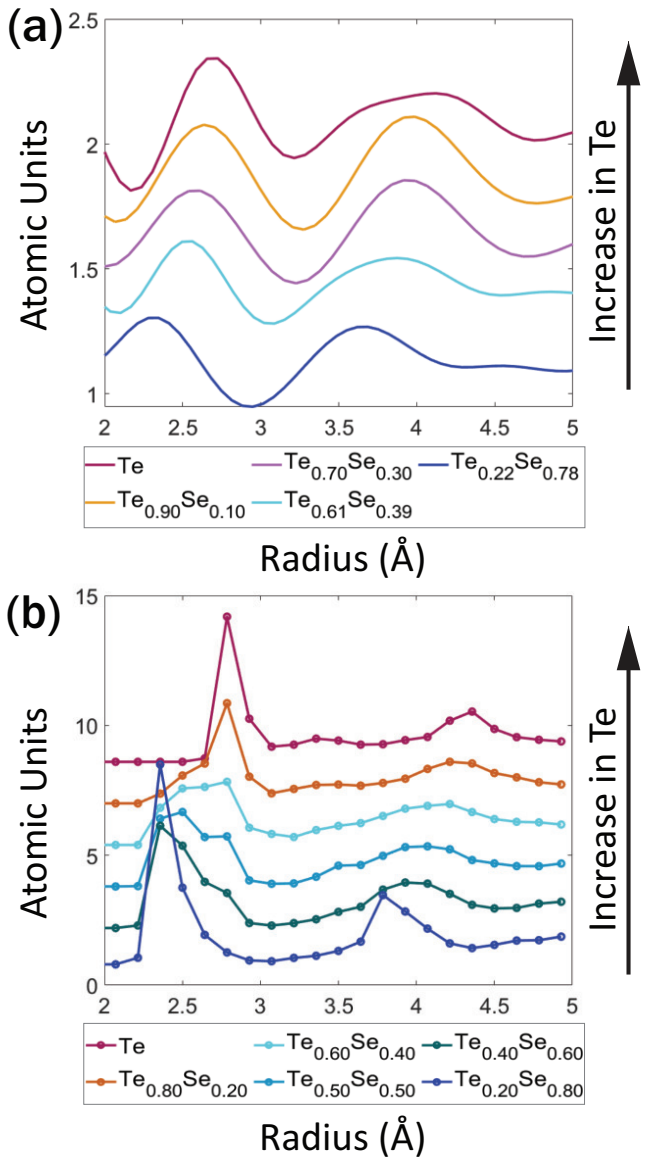


Figure 2.1: Radial distribution function of $Te_xSe_{1-x}$ with compositions of $x = 0.22, 0.61, 0.70, 0.90, 1$ obtained from (a) electron diffraction (b) DFT calculations.

Previous diffraction and spectroscopy studies have shown that amorphous Se (Te) has two nearest neighbor atoms, at a distance of 2.32 Å [60, 61, 62] (2.79 Å [28]), corresponding to the peak observed in the RDF plots at R(Å) $< 3.0$. These distances are close to twice the covalent radius of Se and Te, 1.16 Å and 1.36 Å respectively [63]. The measured RDF peak locations are also similar to the first and second neighbor distances of the Te and Se crystal structure, shown in Fig. 2.2. While the first peak position varies roughly from the value of the first neighbor distance

of crystalline Se at $x = 0.2$ to that of crystalline Te at $x = 1$ , the position of the second peak seems to represent a mixture of the second and third neighbor distances.

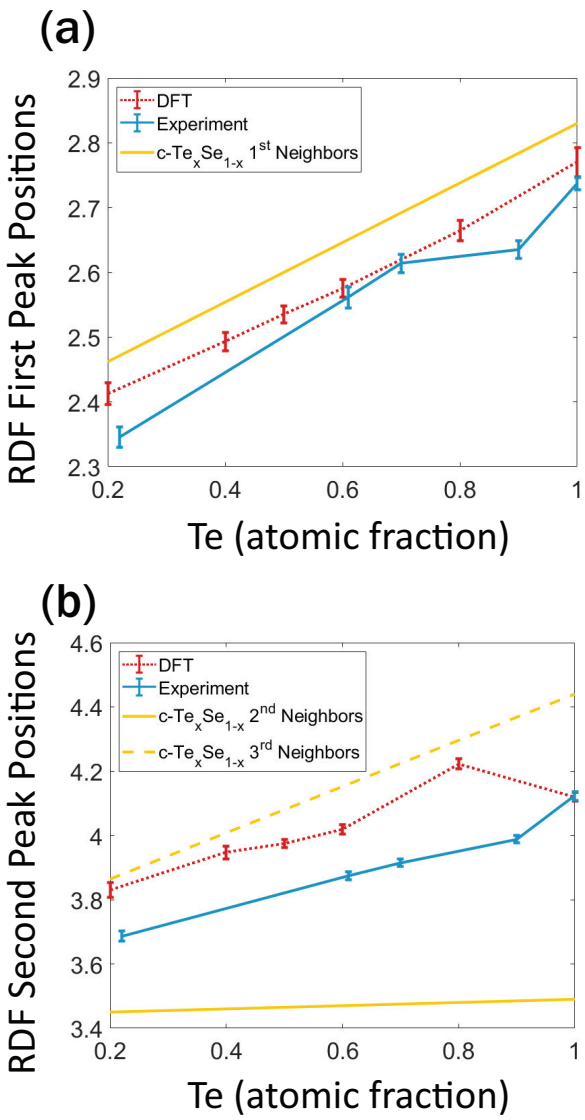


Figure 2.2: Position of (a)the first and (b) the second RDF peaks obtained from the experiments and an averaging simulated systems of different compositions. Yellow line was obtained by applying Vegard's law to crystalline structures[35].

As can be seen in Figure.2.2, the first nearest neighbor or the intrachain distances are lower than their crystalline counterparts. The difference between distances stems from the increase in the covalent bond strength in the intrachain bonding resulting in the shrinkage of the covalent bonds

in the amorphous state [64, 50]. Figure. 2.2 also shows that the difference between experimentally and computationally obtained RDF peak positions is bigger for the second peak than for the first peak. The dissimilarity in the peak position differences is predicted to come from the relatively small size of the simulated systems (192 atoms): while the average interatomic distance is more or less constant in low-energy points of the configuration space, bigger systems may be needed to better reproduce the second-neighbor distance.

Although the spatial resolution is improved in electron diffraction compared to neutron and X-ray diffraction, electron diffraction is subject to multiple scattering effects. While for a typical polycrystalline specimen, multiple scattering does not significantly affect the positions of peaks in RDF measurements, it does affect the coordination number calculations [31]. Because of this, we obtain coordination numbers from our simulations. DFT simulations show that for every composition, the quenched systems also exhibit a chain-like structure. When a bond length of 3 Å was considered, more than 85% of the atoms have a coordination number of 2. Previous computational studies have shown that Se and $Se_xTe_{1-x}$ alloys consist of polymeric chains and $Se_8$ ring elements, their relative fractions depending on the thermal history in the glassy state [65, 66, 67]. Our DFT and RDF results also indicate that the amorphous alloys adopt a chain-like structure, with covalent bonding to the first nearest neighbor distances.

To develop an understanding of the local changes and medium-range orders in the alloys, FEM data was collected (Figure. 2.3). Two distinct peaks, centered around $3.5\,\mathrm{nm}^{-1}$ (solid line) and $4.1\,\mathrm{nm}^{-1}$ (dashed line), are observed. The second peak at $4.1\,\mathrm{nm}^{-1}$ only appears in films with higher Se content. Based on the interatomic distances in RDF analysis extracted from experiment and simulation, the peaks correspond to the intrachain distances of Te-Te and Se-Se. The Te-Te and Se-Se bond lengths in a crystal are plotted as grey lines on the variance curve in Figure. 2.3.

The FEM data therefore indicates that that amorphous structure is composed of at least two types of MRO: an MRO dominated Te-Te atomic interactions and an MRO dominated by Se-Se interactions. This gives rise to two populations of MRO in the thin films: one with bond lengths similar to Te-Te bonds, and one with bond lengths similar to Se-Se bonds. We did not see an evidence of ordering with bond lengths characteristic of Se-Te bonds. Interestingly, as Te concentration increases the intensity of the peak designated as Se-Se intrachain distance decreases, disappearing at Te concentrations above $x > 0.61$ . However, the opposite is not true: MRO corresponding to Te-Te bond lengths remains for Se concentrations up to $x = 0.78$. In addition, the MRO of these alloys do not show significant change below $x < 0.22$ as can be shown in SM Figure 2.7. We assume that as the composition is closer to pure Se, the amorphous structure becomes more homogeneous, and heterogeneities are not substantial.

Recent work has claimed that Se and Te atoms are randomly distributed throughout the chains with a slight preference for Se-Te bonds [51, 3]. Our work indicates that the MRO in Se-Te amorphous films adopts bond lengths characteristic of either Se-Se or Te-Te. Other work has shown that Te fragments consisting of more than two Te atoms lead to the formation of microcrystalline structures [49], which may explain why the Te-Te type MRO remains even at high Se concentrations.

To better interpret the FEM data, partial RDFs were obtained for all compositions from the DFT calculations. Se-Se, Te-Te and Se-Te bond lengths obtained from DFT calculations are plotted alongside the experimental MRO peak positions extracted from the FEM plots. The peak positions

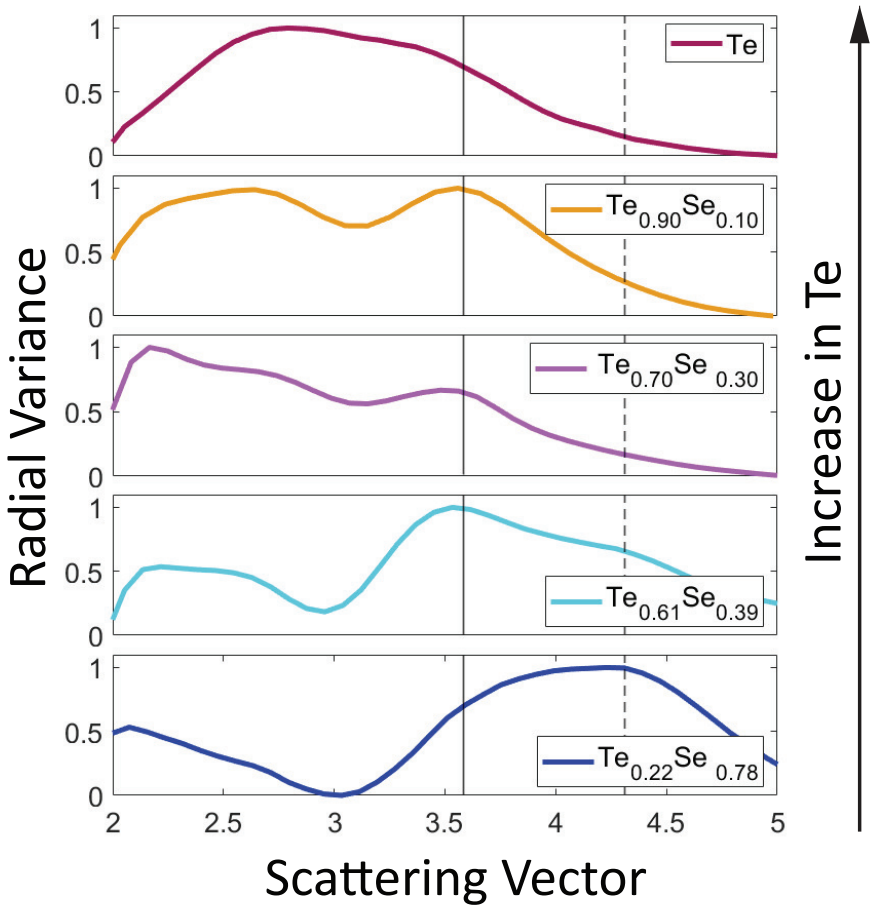


Figure 2.3: Normalized variance curves of $Te_xSe_{1-x}$ with compositions of $x = 0.22, 0.61, 0.70, 0.90, 1$ , show two main peaks placed at $3.5\,nm^{-1}$ as straight line and $4.2\,nm^{-1}$ as dashed line corresponding to the intrachain bond lengths of Te-Te and Se-Se, respectively.

of two MRO populations in the FEM plots agree with the DFT result as shown in Figure. 2.4. Note that as the Te concentration increases, the Te-Te bond distance increases, while the Se-Se bond distance remains almost unchanged in both computational and experimental results.

We attribute the observed changes in the interatomic distances to the bonding in chalcogenides. The crystalline form of both Te and Se is composed of four valence p-electrons, two of which bond covalently, leaving a lone-pair (LP) at the top of the valence band [68], with atomic chains with helical conformations placed parallel on a 2D hexagonal lattice. It has been shown that this helical conformation is affected by the intrachain interaction of neighboring atoms with fully occupied LP orbitals [68]. Although intrachain bonding both in Te and Se are covalent, the main difference between the Te and Se crystals is believed to be the nature of their interchain interactions: For Te, most previous work concludes that this bonding is of a mixed van der Waals and covalent nature,

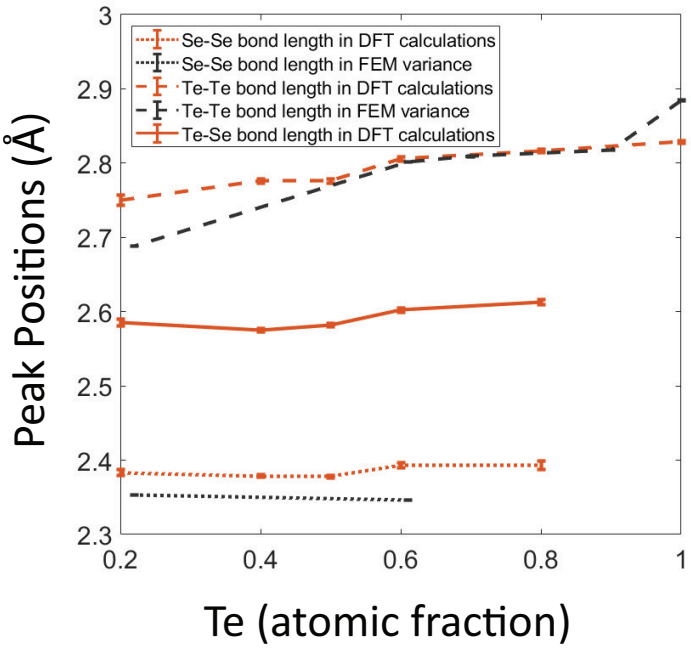


Figure 2.4: The peak positions corresponding to Se-Se (dotted line) and Te-Te (dashed line) bond lengths for all compositions which are extracted from FEM and DFT results.

while in Se crystals it is traditionally assumed to be a weak vdW bond. In fact, the ratio of the nearest interchain to the intrachain covalent bond length is 1.21 for and 1.45 for crystalline Te and Se, respectively[34], suggesting that the interchain bonding in Te is stronger than Se. This is believed to be a due to the lone pairs of electrons of Te atoms participate in forming coordinated covalent bonds between neighboring chains. In addition, crystalline Se has more pronounced covalent character of binding than crystalline Te [69, 70]. For this reason, as the Te concentration increases, the covalent bond strength between first nearest neighbors decreases.

In addition to the intrachain interactions in the local ordering, higher order correlations are attributed to the first peak in FEM plots at $2.6\,\mathrm{nm}^{-1}$ - $2.7\,\mathrm{nm}^{-1}$. Although there is still not enough information regarding the interchain correlations in Se-Te alloys, it is shown that amorphous Se has six second neighbors at about 3.69 Å and this number is increased to 4.23 Å for pure Te [62, 28]. However, it is still challenging to extract the interchain atomic correlations without including the intrachain bond contribution. In this respect, only qualitative observations can be made from the variance plots. As shown in the Figure. 2.3, there is an increasing trend in their relative intensities as Te content is higher. Since the chain to chain bonding strength is higher in Te due to the unlocalized electrons, this might also be an indication that the interchain contributions increases as the glass contains more Te content.

Since Te-Se alloy forms a solid solution for all compositions, we assumed a similar glassy state.

However, as the Te concentration is higher, more MRO associated with Te-Te bond length forms, suggesting that the system prefers to form homopolar bonds. This may lead to the formation of micro crystalline structures [49] or Te phase separation [3].In addition to this, interchain bonding becomes stronger when Te is added. A stronger interchain bonding results in a decreased energetic requirement when establishing the polymeric chain, making alloys with higher Te content more prone to crystallization.

## 2.4 Conclusions

In this study we investigated structural heterogeneity in $Te_xSe_{1-x}$ for a large composition range, including pure Te, at the first time by combining electron microscopy with DFT calculations. Alloys with $x > 0.4$ have not previously been analyzed using electron diffraction methods, and there are no studies have used FEM to characterize MRO in the TeSe system. We observed that the interatomic bond lengths extends as Te is added. In addition, we showed that the intrachain distances are lower than their crystalline counterparts as a consequence of the increase in the covalent bond strength in amorphous films. Finally, we supported our experimental findings with DFT calculations and showed that MRO in the system is affected by the covalent bond strength in Te-Te and Se-Se intrachain bonds. DFT calculations also showed that the structure is chain-like structure with a coordination number of 2. To observe the ordering beyond the short range order, FEM measurements were performed. FEM measurements indicated that the portions of the film with nanoscale ordering have bond lengths corresponding to Se-Se or Te-Te covalent bond lengths, indicating that these regions are rich in Se and Te, respectively. The Te-Te type of MRO was observed in all film concentrations, while the Se-Se type vanished in high Te concentration films.

## 2.5 Supplemental Materials

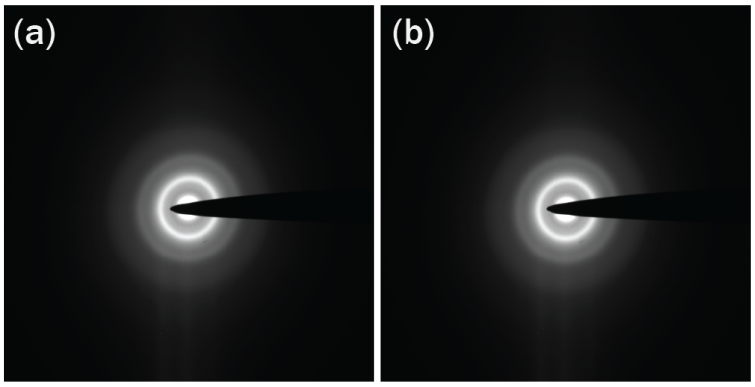


Figure 2.5: Parallel Diffraction Pattern of amorphous Te (a)before and (b) after scanning nanodiffraction experiment

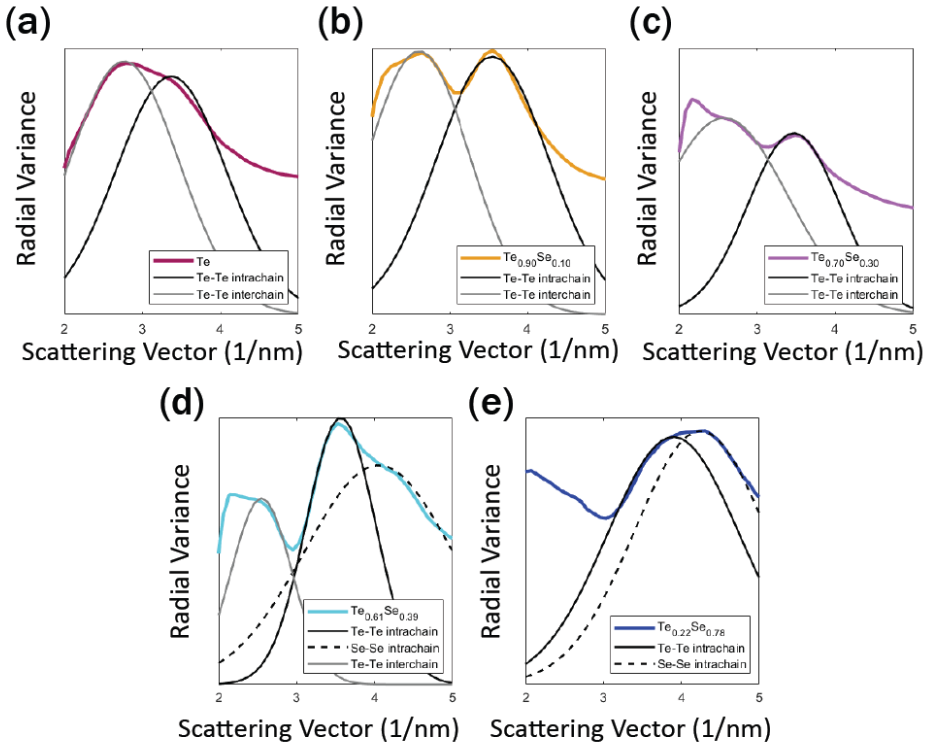


Figure 2.6: Gaussian function curves for obtaining the peak positions of the variance.

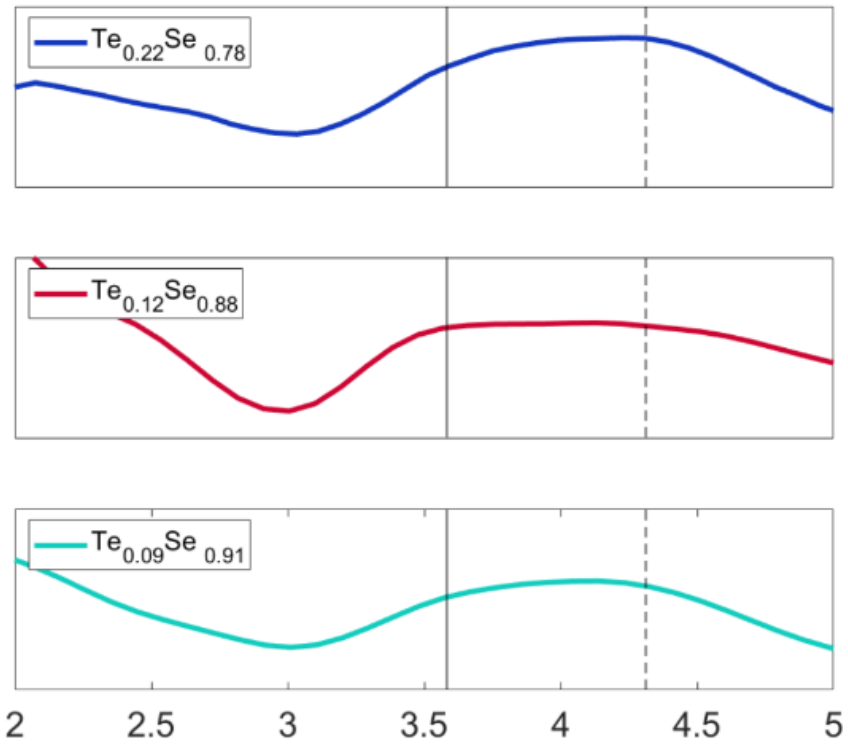


Figure 2.7: Radial variance curves of $Te_xSe_{1-x}$ with compositions of $x = 0.09, 0.12, 0.22$

# Chapter 3

# Analysis of strain and defects in Tellurium-$WSe_2$ moiré heterostructures using scanning nanodiffraction

In recent years, there has been an increasing focus on 2D non-graphene materials that range from insulators to semiconductors to metals. As a single-elemental van der Waals semiconductor, tellurium (Te) has captivating anisotropic physical properties. Recent work demonstrated growth of ultra thin Te on $WSe_2$ with the atomic chains of Te aligned with the armchair directions of substrate using physical vapor deposition (PVD). In this system, a moiré superlattice is formed where micrometer-scale Te flakes sit atop the continuous $WSe_2$ film. Here, we determined the precise orientation of the Te flakes with respect to the substrate and detailed structure of the resulting moiré lattice by combining electron microscopy with image simulations. We directly visualized the moiré lattice using center of mass-differential phase contrast (CoM-DPC). We also investigated the local strain within the Te/ $WSe_2$ layered materials using scanning nanodiffraction techniques. There is a significant tensile strain at the edges of flakes along the direction perpendicular to Te chain direction, which is an indication of the preferred orientation for the growth of Te on $WSe_2$. In addition, we observed local strain relaxation regions within the Te film, specifically attributed to misfit dislocations, which we characterize as having a screw-like nature. The detailed structural analysis gives insight into the growth mechanisms and strain relaxation in this moiré heterostructure..This chapter expands and borrows from what is said in Ref.[71].

## 3.1 Introduction

Two-dimensional (2D) materials research has undergone explosive growth in the past decade, with applications in flexible electronics and optoelectronics [72], catalysis [73], biomedicine [74], and environmental science [75]. More recently, further breakthroughs came from stacking and/or twisting two or more layers of 2D materials. This creates what are known as moiré lattices, which exhibit periodic length scales larger than that of the atomic lattice spacings [10]. Thanks to the in-

troduction of this new periodicity, these materials show considerable deviations from their expected electronic, optical, and magnetic phenomena, such as flat bands, moiré excitons, surface plasmon polaritons, interlayer magnetism, superconductivity, and 2D ferroelectricity [76, 77]. Various two-dimensional (2D) materials have been studied by stacking the same, or different 2D crystals to produce functional devices [72, 76]. 2D materials such as as graphene, hexaboron nitride, and transition metal dichalcogenides (TMDCs) can act as building blocks for these heterostructures, creating a nearly infinite design space for moiré heterostructures.

Although the ability to tune a heterostructure's optoelectronic performance as two or more layers are stacked is desirable, the strain transfer between different van der Waals layers is expected to induce dramatic changes in a material's electronic, quantum transport, and photonic performance as the complexity of the structures increases [12, 11, 13]. In order to scale up the applications of such heterostructures, there is a great need to understand how strain develops and relaxes during thin film growth and how it behaves after the growth. Although the primary strain relaxation mechanism in heterojunctions is the formation of misfit dislocations, there are additional strain relaxation pathways for 2D films. Recent experimental works suggest that misfit dislocations alone cannot account for the measured strain relaxations in heterostructures such as tungsten disulfide $WS_2$, tungsten diselenide $WSe_2$, graphene, and boron nitride (BN). Instead, out-of-plane ripples play an important role in compensating the local strains [78, 79]. Moreover, de Jong et al. demonstrated that moiré lattices show subtle distortions due to local variations in twist angle and interlayer strain. They also found that the moiré lattice could play a role in stabilizing these defects by minimizing the local stacking fault energy within the moiré unit cell [80]. Therefore, mapping local strain and defect concentration is an important step towards fully understanding the behavior of heterostructure materials.

Recently, Te thin films have been used in electronics, optoelectronics, energy devices, and sensors due to their inherent structural anisotropy, high hole mobility, and large photoconductivity [81, 82, 6]. Distinct from 2D van der Waals materials such as TMDCs, crystalline Te is composed of an array of covalently bonded parallel atomic chains on a two-dimensional (2D) hexagonal lattice parallel to the $[0001]$ direction. The bonding between the nearest-neighbor atoms between the chain is weak van der Waals (vdW) bonding. The appealing properties of tellurium such as anisotropic carrier mobility [83], thermal conductivity[84] mechanical and electromechanical properties [85] have fueled a resurgence of interest in synthesizing ultrathin Te films. X. Huang et al., demonstrated that when monolayer tellurium is placed on a graphene substrate (with the tellurium chains aligned parallel to the graphene surface), it exhibits a significant band gap of around 1 eV. As the thickness of tellurium increases, the band gap gradually decreases and approaches the bulk value of 0.34 eV [7]. This axis and thickness-dependent behavior suggests new possibilities for tuning the optical and electronic properties of tellurium-based materials for real devices and thin film applications. G. Hao et al. stated that ultrafast solid-state lasers, along with all-optical modulation and various other nonlinear devices, can be developed by leveraging Te-Transition metal dichalcogenide (TMDC) heterostructures [86]. Research and development in low-dimensional tellurium production are ongoing to explore and understand the full potential of these materials for various technological applications. As the demand for advanced electronic and optoelectronic devices, energy storage solutions, and efficient catalysts increases, the significance of low-dimensional tel-

lurium materials will likely continue to grow. However, the in-plane orientation of the Te crystal on most substrates is random. Previously, we demonstrated van der Waals epitaxial growth of 2D Te flakes with thickness down to 5 nm on the surface of 2D transition metal dichalcogenides (TMD) $WSe_2$, $WS_2$, $MoSe_2$, $MoS_2$ flakes. In the case of $WSe_2$, the *c*-axis of Te is aligned with the armchair direction of the substrates[9]. The ability to control the growth direction of the Te thin films is exciting, however it is still necessary to understand the strain and strain relaxation mechanisms which may alter the behavior of this system.

The formation of a moiré structure can lead to two distinct scenarios: one wherein the two layers share a mutual (expanded) periodicity, and the other wherein they do not. Moiré structures with a mutual periodicity are termed "commensurate", and aperiodic structures are designated "incommensurate". Incommensurate and commensurate structures can coexist within the same system simultaneously. In addition to these moiré structures, approximate periodicities may be present, e.g. rational approximates of an irrational periodicity may be observable. These periodicities are also experimentally observable, and we term them "approximate tilings". Various characterization techniques are employed to reveal moiré lattices with varying length scales,including convergent beam electron diffraction (CBED)[87], scanning tunneling microscopy (STM)[88], atomic force microscopy (AFM)[89], and differential phase contrast (DPC) and four dimensional-scanning transmission electron microscopy (4D-STEM) [90]. Out of these methods, 4D-STEM, which records a 2D image of the diffracted electron beam at each probe position, gives unique information about the moiré lattice structure, orientation, and structure-dependent properties[20, 19]. 4D-STEM can also be used to map the strain fields, allowing a large field of view and flexibility with regards to sample type and orientation.

In this paper, we performed a detailed analysis of the $WSe_2$-Te system to study the structure and orientation of the moiré lattice formed due to the interaction between the substrate and the film. We determined the precise orientation of the Te flakes with respect to the substrate by combining electron microscopy with image simulations, showed that Te chains are aligned along the armchair direction of $WSe_2$, and deduced how the moiré superlattice is formed. We directly imaged the incommensurate moiré lattice and found an approximate periodic tiling which forms a periodic moiré cell with CoM-DPC and STEM imaging. Mapping strain and detecting defects in the films is non-trivial; for this, we used scanning electron nanodiffraction with subsequent strain and defect contrast ($\vec{g} \cdot \vec{b}$) analysis. Our results indicate non-uniform strain in both the Te and $WSe_2$ films, significant rotation in portions of the Te film, and dislocations associated with the rotated regions of the Te film.

## 3.2 Methods

**Materials Growth and TEM specimen preparation** We exfoliated the $WSe_2$ flakes on $SiO_2$/ Si substrates. For the growth of the thin film, we used a two-zone hot wall quartz tube where we loaded the alumina boat containing powdered Te (99.999%, Sigma-Aldrich) as the precursor at one zone and the substrates at the downstream region. We pre-annealed the substrates at 300 $^\circ C$ under Ar flow to produce more uniform and thicker films. After the pre-treatment is performed,

we set the substrate temperature up to 130 $^{\circ}C$ for growing the Te on $WSe_2$ substrate. More details regarding the growth can be found in our previous article [9]. We transferred the $WSe_2$/Te flakes on a carbon coated TEM grid using a dry transfer method.

**TEM data collection and image simulations** For the bright-field and high resolution TEM (HRTEM) imaging, we used an FEI Titan 60–300 microscope with an acceleration voltage of 300 kV. We determined the thickness of the films and substrate by using electron energy loss spectroscopy on an FEI Tecnai operated at 200 kV with a C2 aperture of 150 µm, a camera length of 42 mm, and an entrance aperture of 2.5 mm. We used the zero-loss peak to calculate the film thickness within the Digital Micrograph software. The Fourier log deconvolution indicated a $t/\lambda$ value of 0.282 from substrate and 0.4235 from the film which correspond to a thickness of $18 \pm 2$nm and $12 \pm 2$nm for substrate and the films respectively.

To find the orientation of the Te flakes with respect to the substrate, we matched simulated HRTEM images and their corresponding FFTs to our experimental HRTEM data using custom Python and MATLAB scripts. First, we constructed Te crystals with different zone axes and in-plane orientations on the substrate and performed HRTEM image simulations using the abTEM simulation package [91]. After we found the in-plane orientation of Te with respect to $WSe_2$, we studied the structure and orientation of the moiré lattice. We generated a super cell with Te ($a = 4.456$Å$, c = 5.921$Å)[92] and $WSe_2$ ($a = 3.282$Å$, c = 12.96$Å)[93] crystals. To replicate the experimental FFTs, we oriented Te along $< 2\bar{1}\bar{1}0 >$ and tilted $WSe_2$ along $< 0001 >$ zone axes. Then, we rotated the Te crystal along the out-of-plane(z) axis to align the chains along one of the armchairs of $WSe_2$. After we made the supercells, we simulated HRTEM and corresponding fast Fourier transform (FFT) images. By iterating the image simulation parameters which are the rotation, x and y shifts, shear, and thickness of layers, we found the output cell parameters shown in Table (3.1) and how many cells were needed to generate the moiré lattice. Our best-fit estimate for the overall thickness is 34 nm, which is composed of 12 layers of $WSe_2$ (15.5 nm) and 24 layers of Te (18.7 nm). The thickness values derived from iterative simulations represent the optimal conditions for accurately reconstructing and identifying the moiré lattices according to the experimental FFT. The reconstruction involved adjusting the thickness until the best fit was achieved, yet the resulting intensities exhibit only a weak dependence on the thickness. This is because our reconstruction code primarily focused on accurately determining the position of the Bragg peaks, specifically aimed at solving for the moiré unit cell. The thickness needs only to be sufficiently large to accommodate multiple scattering contributing to the moiré peaks observed in our experimental measurements. Consequently, the simulated cell might tend towards larger thicknesses. However, our rigid model did not account for these effects caused by local strain, which introduces deviations from the ideal moiré condition. As a result, the intensities and, consequently, the layer thicknesses are likely to exhibit significant disparities. It is important to note that the provided thickness is an approximation, with the understanding that EELS measurements offer a more reliable determination of the material's true thickness.

**DPC imaging** We collected 4D-STEM data for DPC measurements on the double-aberration-corrected TEAM 0.5 microscope with the 4D Camera, developed in-house in collaboration with Gatan Inc. The 4D Camera is a direct electron detector with 576 x 576 pixels and a frame rate of 87 kHz. We collected 4D-STEM data at 80 kV with a 25 mrad convergence semi-angle, a beam

current of 52 pA, estimated from 4D camera counts. The real-space pixel size is 0.61 Å, and camera reciprocal space sampling of 173.6 µrad per pixel [94].

**Scanning nanodiffraction data collection and analysis for strain mapping** We collected scanning nanodiffraction data on the double-aberration-corrected TEAM I microscope operated at 300 keV with convergence angle of 0.9 mrad, a step size of 2 Å, and a camera length of 130 mm. We used bullseye apertures to improve the precision of the detected peak positions [95] (SI Figure 3.8(d)). We utilized the py4DSTEM package for the data calibrations and strain mapping analysis [20]. Calibrations include correcting shifts of the diffraction pattern, calibrating the rotational offset between real and diffraction space, and calibrating the pixel sizes. After we performed the calibrations, we detected the Bragg peaks from each of the data points to obtain Bragg vector maps (BVM) (SI Figure 3.8 (e),(g)). Then, we extracted the average reciprocal lattice vectors and indexed them for $WSe_2$ and flakes differently. We defined one of the basis vectors to be aligned along the Te c-axis, and the other to be perpendicular to the chains. We defined the reference lattice as the median measured lattice constants of $WSe_2$ and Te. Then, we computed the infinitesimal strain tensor at each beam position by examining the deviation of their local lattice vectors.

**Virtual dark field image analysis** To visualize the dislocations and find the Burgers vector for the dislocations, we performed virtual imaging from the scanning nanodiffraction data set. We placed virtual detectors around the specific Bragg disc positions and averaged the diffraction patterns to generate virtual dark field images.

## 3.3 Results and Discussion

The overview TEM images and diffraction data shown in Figure 3.1 confirm the preferential growth direction of the tellurium flakes on the $WSe_2$ substrate. They typically have one smooth facet termination and jagged edges along the $< 0001 >$ direction, as shown in Figure 3.1 (a). The thickness of the flakes is about $12 \pm 2$nm. The Bragg peaks corresponding to each material in the SAED pattern are shown in Figure 3.1 (c), with Te Bragg peaks labeled as pink, and $WSe_2$ in blue. The HRTEM data in Figure 3.1 (b) and the SAED data in Figure 3.1 (c) indicate that the Te and $WSe_2$ films are aligned with the $< 2\overline{1}\overline{1}0 >$ and $< 0001 >$ zone axes along the beam direction Figure 3.2(a). The relative orientation of the Te and $WSe_2$ films is consistent with our previous observation that the Te chains are aligned with the armchair direction of the $WSe_2$, due to the relative binding energies of the materials [9]. We show the orientation of $WSe_2$ and Te in Figure 3.2 (b) where the two atomic structures overlaid in the middle part of the simulated super cell structure.

In addition to the main Bragg peaks of both phases, there are extra intensity modulations generated by the interaction between $WSe_2$ and Te films (Figure 3.1 (c)) shown as yellow circles. We also observed satellite peaks associated with the Bragg peaks indicated by yellow circles in Figure 3.1 (c). These peaks, are highlighted within the yellow squares in Si Figure 3.5. The peaks with the larger periodicity correspond to an incommensurate moiré lattice formed between the Te and $WSe_2$ films, which is represented by purple arrows Figure 3.5 (b). Similarly, the peaks indicating

a smaller periodicity, highlighted by yellow circles in Figure 3.1 (c) and corresponding to the main Bragg peaks visible in SI Figure 3.5 (b), are attributed to an approximate periodic tiling.

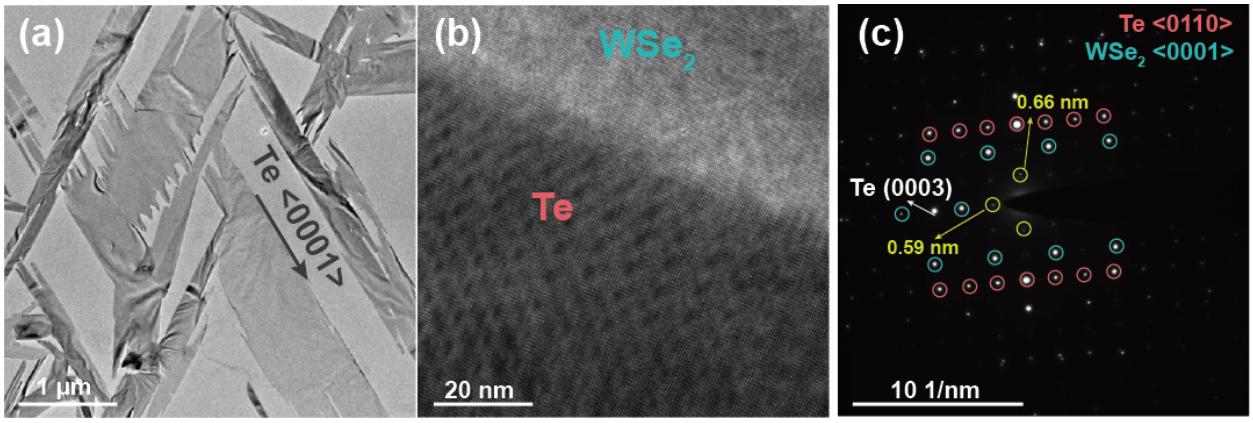


Figure 3.1: a) Bright field image of the Te flakes on $WSe_2$ substrate. b) HRTEM images showing the moiré lattice c) SAED pattern collected from the HRTEM region shown in b).The yellow circles indicate the additional modulations that result from the approximate tiling.

The relative dimensions of the observed incommensurate moire lattice and the smaller approximate tiling are shown in SI Figure 3.6. The smaller, visibly periodic pattern, or approximately periodic tiling, which constitutes the dominant visual feature in experimental observations (as shown in 3.1 (b) and (c), emerges due to the minimal separation between the true tiling and its approximate counterpart. This phenomenon is illustrated by the yellow circles in SI Figure 3.6(a) and (b), a consequence of illustrative rendering, and in our diffraction and other datasets, owing to the physical dimensions of atomic potentials. The moiré periodicity associated with the specific angle of this system is comparatively large, necessitating a broader field of view for visibility, as depicted by the purple circles in SI Figure 3.6 (c). To elucidate the expansion of the incommensurate moiré lattice, we further illustrate the larger periodicity inherent in the approximate tiling, as shown in SI Figure 3.6 (d).

To directly visualize the outcome of the tiling in real space with atomic resolution, we utilized a combination of HRTEM imaging, HRTEM simulation, and DPC/STEM. Atomic resolution DPC imaging relies on the deflection of the focused beam by the electrostatic potential of the atoms in the sample [20]. Figure 3.2 (c) shows CoM-DPC images that indicate the approximate periodic tiling, consistent with the d-spacing of the extra peaks (yellow circles) observed in the SAED in (Figure 3.1 (c)). We also showed the same periodicity on Figure 3.2 (b) with a solid square.

In addition to the extra intensity modulations formed due to the the approximate periodic tiling, we detected incommensurate moiré superlattice in HRTEM images (Figure 3.1 (b) and Figure 3.2(f)) and faintly visible in CoM-DPC/STEM image Figure 3.2 (c). We confirmed the observation of this periodicity by the satellite peaks appearing in the fast Fourier transform shown in Figure 3.2 d) and inset in SI Figure 3.5 (b).

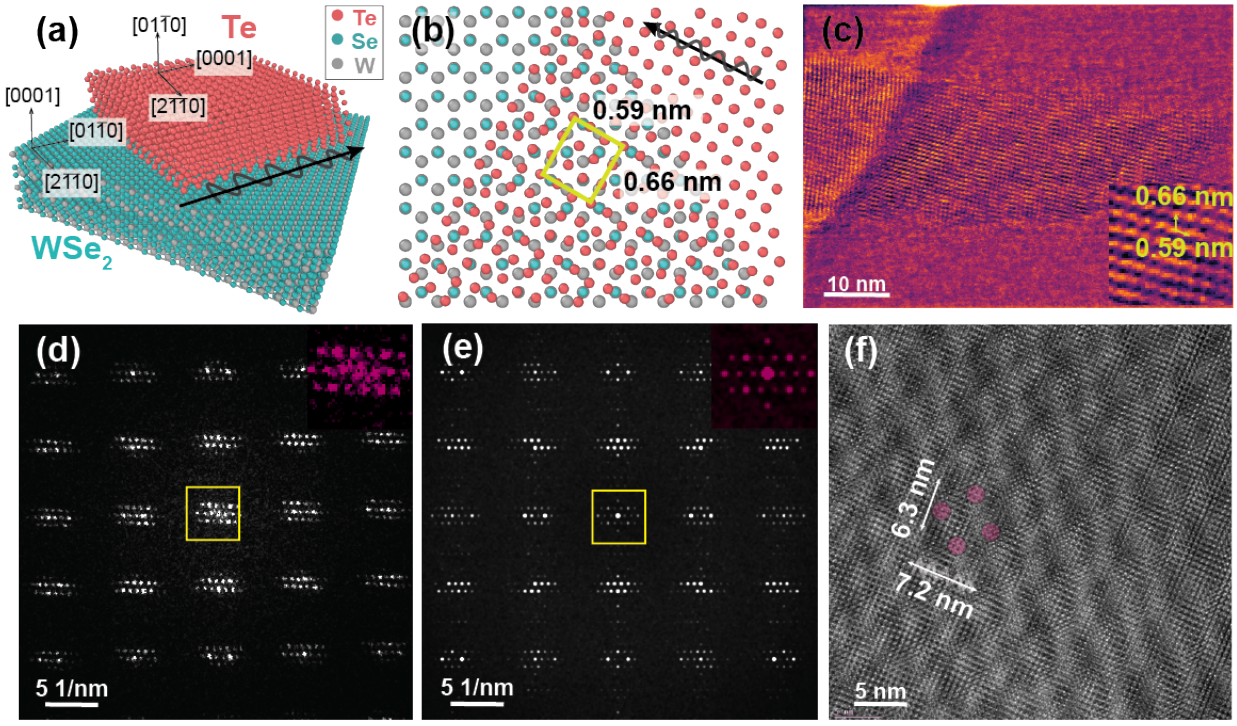


Figure 3.2: a) Schematic of the aligned Te deposited on $WSe_2$. Pink atoms represent Te, green Se and gray W. b) Atomic configuration between Te atomic chains and $WSe_2$ surface where the c-axis of Te is parallel to the armchair direction of $WSe_2$. Yellow square shows the approximate tiling. c) CoM-DPC image indicate the periodic patterns of the approximate periodic tiling. d) FFT of the HRTEM image in f). Inset shows the magnified image of the center part of the FFT. e) FFT of the simulated HRTEM image. f) HRTEM image showing the moiré lattice with two basis vectors with a length of 7.2 nm and 6.3 nm

To unravel the structure and orientation of the two films that form the moiré lattice, we performed a two-stage image simulation. Electron microscopy observations established the relative in-plane orientation of the materials. The specific orientation of tellurium was determined through controlled rotation along the c-axis to facilitate the determination of smaller periodicity via image simulations. Then, an iterative fitting simulation incorporated experimental data and prior simulations to solve for the most accurate relative positions of the two materials and thereby determined the moiré structure. Through iterative image simulations, we adjusted parameters like rotation, strain, shear, and thickness of the Te and $WSe_2$ films. The simulated Fast Fourier Transform (FFT) images remained unaffected by aberrations and material constraints. (Figure 3.2 (e). We reported how Te and $WSe_2$ unit cells must be stacked in terms of rotation and lengths in Table 3.1. According to iterative simulation results, the best approximate match we found to form the moiré lattices at the larger scale which is shown in the HRTEM image in Figure 3.2 (f) is to repeat Te unit cell

19 times along $< 2\bar{1}\bar{1}0 >$ axis, 12 times along $< 01\bar{1}0 >$ axis and $WSe_2$ unit cell 14 times along $< 2\bar{1}\bar{1}0 >$ axis, 12 times along $< 0001 >$ axis. Iterative fitting yielded a rotation of 0.14 degrees and minor strain in satellite peak rows within the experimental FFTs to construct the incommensurate moiré lattice from the cell parameters. Notably, moiré satellite peak positions exhibited complex dependence on the parent lattice. Each peak "cluster" displayed slight rotational shifts, with significant internal cluster rotation. Supplementary SI Figure 3.7 visually presents the simulated FFT and reciprocal lattices (SI Figure 3.7(c) and (d)) resulting from iterative simulations, originating from the experimental FFT SI Figure 3.7(a).

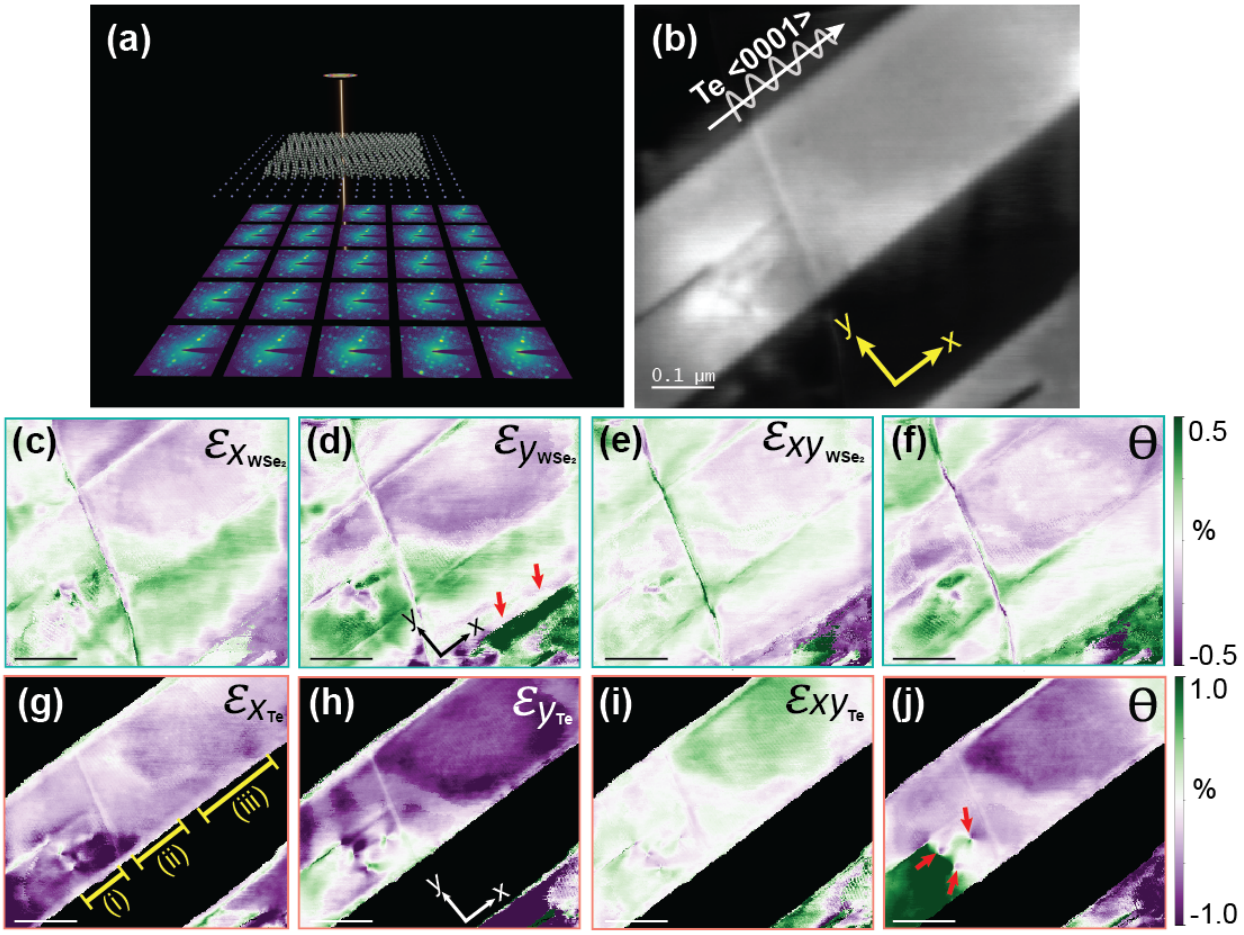


Figure 3.3: a) Sketch of experimental setup for 4D-STEM strain mapping. A converged electron probe is rastered across the sample and a diffraction pattern is collected for each position. b) HAADF image of the flake and the substrate. Strain maps generated from c-f) $WSe_2$ and g-j) Te lattices.We defined the reference lattice as the median measured lattice constants of $WSe_2$ and Te, and used these values to calculate the relative strain values. The x and y components of the strain, whose direction is illustrated in b), d), and h), correspond to the $< 0001 >$ and $< 1\bar{2}10 >$ directions of the Te lattice and the $< 2\bar{1}\bar{1}0 >$ and $< 01\bar{1}0 >$ of the $WSe_2$ lattice. Scale bar is 0.1 µm

Table 3.1: Crystallographic directions corresponding to the axes of the orthogonal supercell used for simulations, with the corresponding cell dimensions. The electron beam propagates along the *c* direction of the cell. All dimensions are in Å

| Material | a | b | c |
|---|---|---|---|
| $WSe_2$ | $(2\bar{1}\bar{1}0)$<br>3.3270 | $(01\bar{1}0)$<br>5.7625 | $(0001)$<br>12.9600 |
| Te | $(2\bar{1}\bar{1}0)$<br>4.5152 | $(0001)$<br>6.0026 | $(01\bar{1}0)$<br>7.8064 |

4D-STEM can detect local changes in the lattice at each scan position by first measuring a 2D diffraction pattern at each probe location (Fig.3.3 (a)). Local strains are then mapped throughout the sample by measuring the infinitesimal change in the lattice with respect to a reference lattice. The results of 4D-STEM strain mapping are shown in Figure 3.3. We generated separate strain maps for $WSe_2$ and Te by first individually detecting their Bragg peak positions, as shown in SI Figure 3.8 (c)(e) and (g), then calculating the local strain for each material from their non-overlapping Bragg peaks to get individual strain maps. (Figure 3.3). The maps of the *x*, *y*, and shear components of the strain tensor, as well as the principle rotation, are shown in Figure 3.3(c-j). Since we are aiming to understand the strain relaxation along Te chain and the direction perpendicular to the Te chains, we calculated the strain components along these two lattice vectors, labeled *x* and *y*, respectively. Therefore, the $\varepsilon_x$ component of strain in each material can be understood as strain along the c axis of the Te, and the $\varepsilon_y$ component is the one perpendicular to the c axis of the Te.

As shown in Figure 3.3 (c-j), the strain solely in the $WSe_2$ layers is lower (±0.5%) than on the Te film (±1%). The strain map shown in Figure 3.3 (d), indicates an in-plane tensile strain along *y* direction at the edges of the Te flakes as shown by the red arrows. This indicates that the van der Waals forces of Te along the direction perpendicular to the chain cannot compensate for the strain generated by the epitaxial growth of Te films. The reason behind this stems from the surface energy difference between different planes Te. The bond strength along the *c*-axis of Te, and hence the surface free energy of the $\{0001\}$ surfaces are between two and three times greater than the corresponding values for the prismatic $\{1010\}$ surface [96]. In order to decrease the surface energy, the surface area of the Te $\{0001\}$ facets are limited. Te crystals, therefore, tend to grow in the form of extended hexagonal prisms or dendrites parallel to the substrate surface. We also observed the same behavior in other Te flakes too as shown in SI Figure 3.9. Another reason for the dendritic growth can be explained from the kinetics point of view: since the Te interchain bonds are primarily of van der Waals character, the edge diffusion will be very rapid relative to the diffusion of Te atoms on a pristine $\{0001\}$ surface on which atoms are covalently bonded to the chains [9]. Therefore, tellurium tends to grow as flakes and have rough $\{0001\}$ facets[97].

Because of the difference in the d-spacings of the substrate and film along the chain ($d_{WSe2}$= 0.571,$d_{Te} = 0.596$)[98, 78], compressive strain is expected to be dominant along x direction (the Te chain direction) in the strain maps. To better understand the strain relaxation mechanisms in the heterostructure, we divided the strain maps into three regions, marked as (i), (ii) and (iii) based on the observed strain and rotations (marked on Figure (3.3(g)). At the region (ii) and (iii) of

the strain map labeled with yellow lines, the Te flake releases the strain through lattice distortions. The periodic lattice pattern that is also visible on both HAADF and the right-end of the strain maps matches the moiré lattice we observed in 3.2(f) and SI Figure 3.8(b),(c).

The leftmost region,region (i), indicated in Figure 3.3(g) shows both a compressive strain of approximately 0.5% and significant rotation (Fig. 3.3(j)). The linear feature that separates the left (i) and middle parts (ii) of the Te flake is visible in the HAADF image (Figure (3.3(b)) and strain maps obtained from the $WSe_2$ lattice vectors (Figure (3.3(c-f)). It is likely either a dislocation or a crack on the substrate. Although we do expect that the substrate releases the strain during the pre-annealing treatment, the substrate may be exposed to stress during the transfer of the substrate and the film to the TEM specimen holder. Furthermore, in our efforts to ensure there was no obvious mechanical damage resulting from the TEM sample preparation, we conducted thorough examinations at both lower and higher magnifications in bright field mode. The strain values we measured for $WSe_2$ substrate and Te are between -0.5 to 0.5 % and -1 to 1 % respectively and we attribute these modest strain values to Te-$WSe_2$ interactions, and expect much higher strain values for mechanically damaged samples. For example, the 5 layers $WSe_2$ can endure 12.4 GPa stress and 7.3% strain without fracture or mechanical degradation [99]. There is an approximately strain-free region at the mid-part region (ii) close to the linear defect, which suggests there is another strain relaxation mechanism than the lattice strain that helps the lattice overcome the stress generated due to the linear feature and rotation of the left part of the flake. After careful investigation on region (i), which contains significant rotation of the Te lattice, we detected misfit dislocations, which can be shown as red arrows on the rotation maps. The misfit dislocations are more easily recognized in the rotation map by observing their dipole fields as in (Figure (3.3(b)) [78]. The dislocations in crystals composing the heterostructure, in the form of moiré pattern dislocations, stems from a missing row of atomic unit cells. The appearance of these dislocations magnifies with the addition of layers. Therefore, moiré pattern dislocations contains similar features as dislocations in Te crystals.

To measure the Burgers vector $\vec{b}$ of the dislocations, we performed virtual dark field image analysis subsequent defect contrast analysis [18]. In Figure 3.4, we demonstrate that the dislocations are visible on planes along the c-axis and perpendicular to the c-axis. However, their contrast disappears for the planes corresponding to the moiré lattice. We found that the $(0\bar{2}22)$ set of planes of the Te lattice are where the dislocations are least visible. From the invisibility criterion of $\vec{g}\cdot\vec{b}=0$, the Burgers vector is parallel to the $<\bar{1}2\bar{1}3>$ direction. This reveals that the burgers vector is one of the most common ones in Te, $\vec{b}=c+a$ [100]. Dislocations which are located in the prismatic planes and lead to a rotation around the $<2\bar{1}\bar{1}0>$ axis, as in our system, are connected with two different dislocation families which are "*c*" screws and one of the three "*a*" screws [101]. However, previous work argues that the invisibility criterion of $\vec{g}\cdot\vec{b}=0$ is not a sufficient condition for the identification of the dislocations in Te due to elastic anisotropy [100]. They added that the condition is only sufficient when the displacement field of the dislocation is parallel to the dislocation line, as in the case of screw dislocations. For this reason, the moiré dislocations we observed in Figure 3.4 likely have a screw character and the burgers vector is not precisely parallel to the beam direction, $<2\bar{1}\bar{1}0>$.

The observed topological dislocations break the translational symmetry of the moiré lattice and

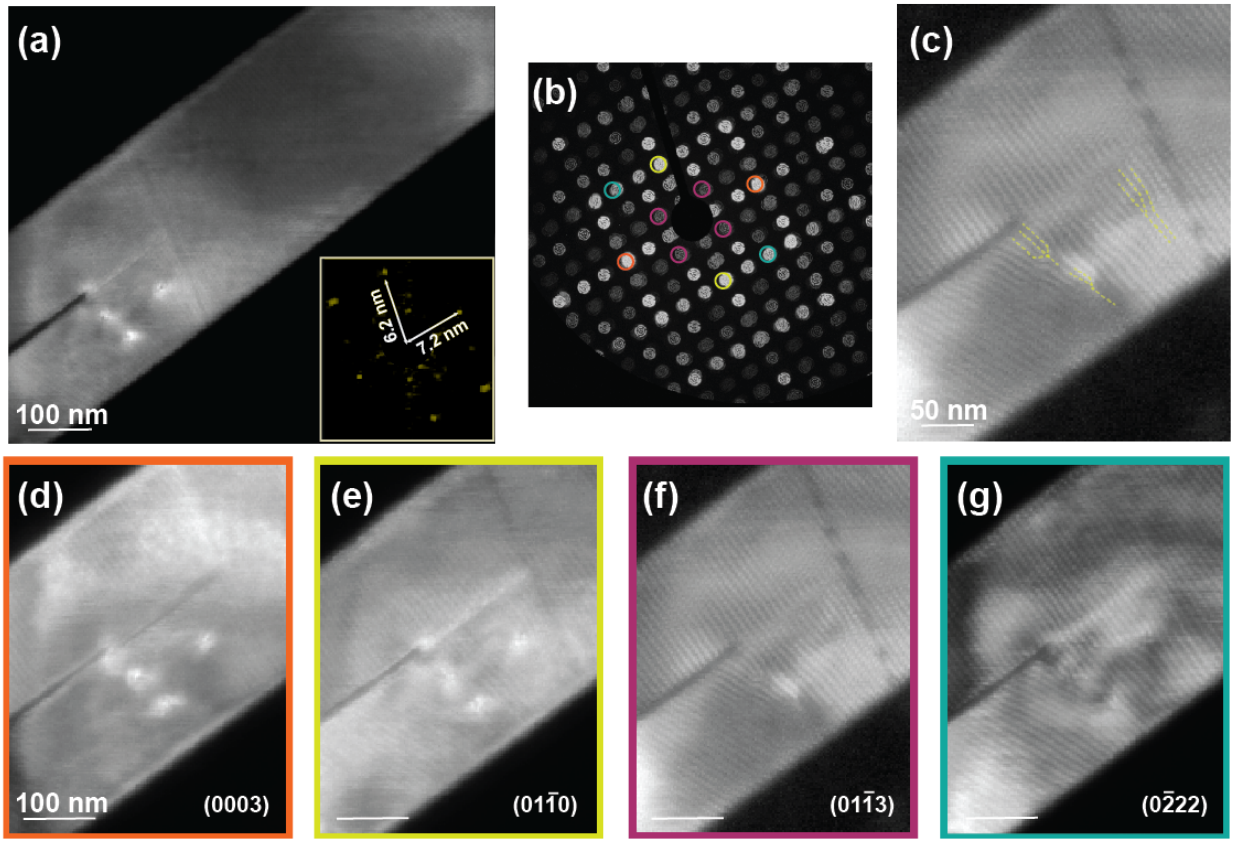


Figure 3.4: a)Virtual dark field image. b) Virtual annular dark-field detectors. c)Virtual dark field image showing moiré dislocations. d-g) Virtual dark-field images corresponding to circular detectors about each of the indexed Bragg peaks.

are expected to alter the properties of the system, for example they may cause a phase difference between the electron paths encircling the defect clockwise and counterclockwise [80]. In addition, the observed strain in $WSe_2$ and Te are known to alter the optoelectronic properties. In the case of $WSe_2$, biaxial strain bends down both the conduction band minimum and valence band maximum at different rates, leading to an overall bandgap narrowing [102]. In trigonal Te , shear (hydrostatic or uniaxial) strain causes the material to change from a trivial insulator to strong topological insulator [103]. Ultimately, both the observed defects and strain will influence the behavior of this moiré heterostructure.

## 3.4 Conclusions

Moiré heterostructures are intensely studied due to the attractive possibility of tuning optoelectronic properties by varying lattice mismatch and orientation. However, defects and strain may

further alter material performance, and it is therefore important to monitor these structural features that may arise during film growth. Here, we examined Te-$WSe_2$ heterostructures using electron microscopy. PVD growth of Te on $WSe_2$ produced thin Te films with chains oriented along the armchair direction of the $WSe_2$. We determined the moiré structure of this system by solving for the orientation of the Te, and used scanning nanodiffraction to measure strain in both materials and detect defects in the Te. The strain and defect formation arise from the lattice mismatch between the two materials, and geometrically necessary defects occur in Te as a part of the film growth process. Ultimately, our findings not only elucidate how moiré structures form due to the interaction between Te and $WSe_2$ materials, but also shed light on new studies on moiré and/or strain engineered layered materials that provides a platform for engineering and manipulating materials to develop functional materials and devices both at macro and nanoscale by using $WSe_2$ and Te materials. This study illustrates how prevalent local structural imperfections can be in van der Waals heterostructures produced by thin film deposition, and point to the possibility of further tuning growth conditions to produce more perfect films. Ultimately, local measurements of defects and strain are important tools to provide insight into the production and performance of van der Waals heterostructures.

## 3.5 Supporting Information

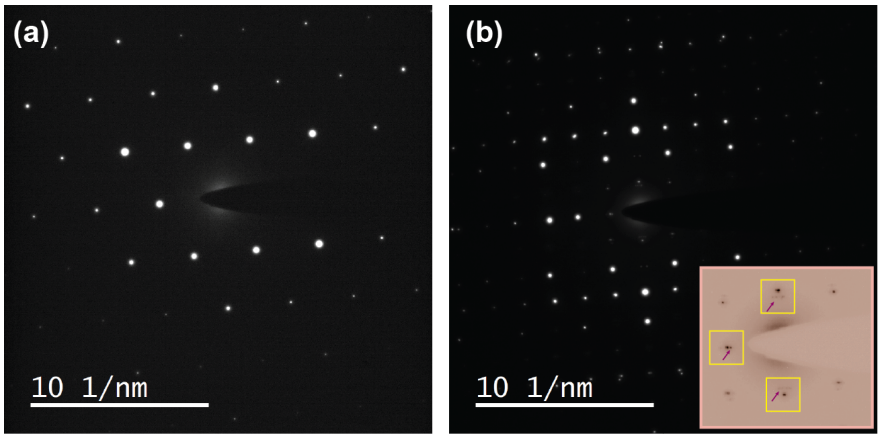


Figure 3.5: a)SAED colected from the $WSe_2$ substrate, b)SAED colected from the flake.The inset displays additional intensity modulations, depicting the approximate tiling as yellow squares, and satellite peaks resulting from the incommensurate moiré lattice, indicated by purple arrows.

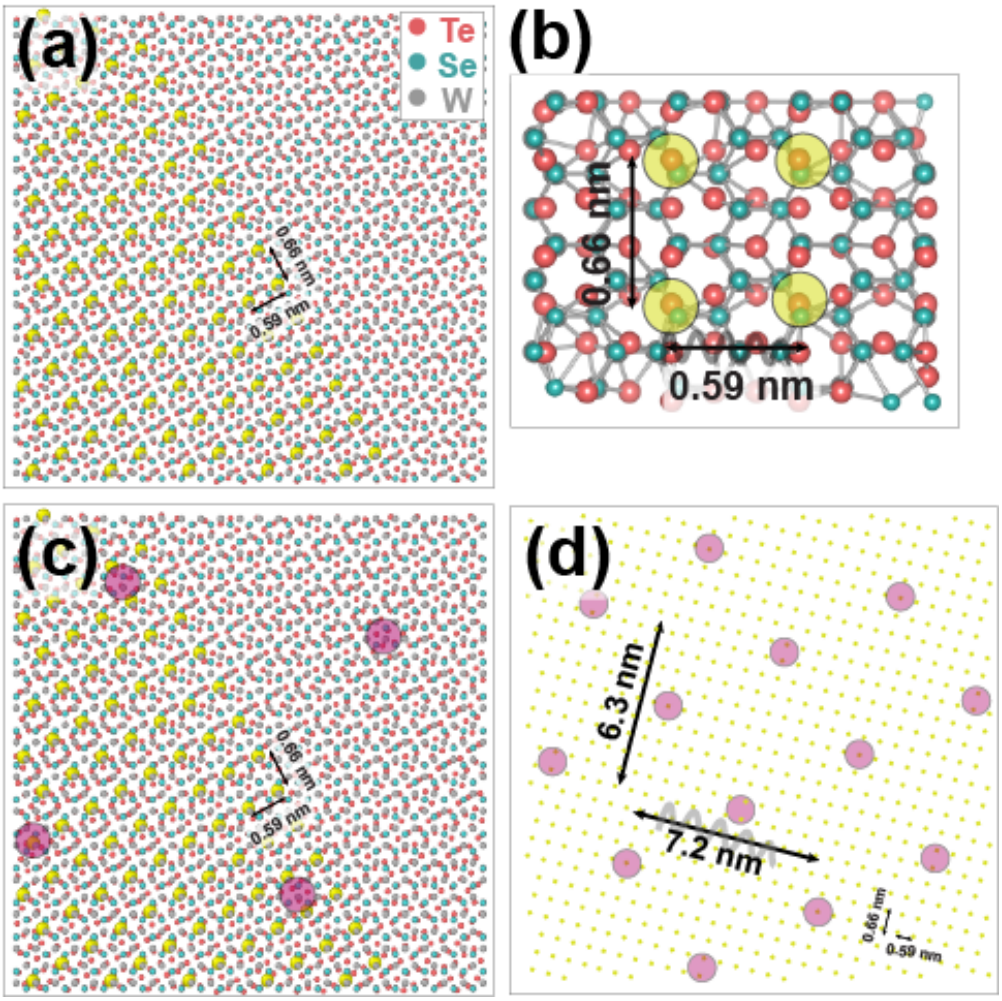


Figure 3.6: a) Simulated cell, measuring 80x80 Angstroms, with the c-axis of Te aligned parallel to the armchair direction of WSe2, illustrating the approximate tiling represented in yellow. b) Atomic configuration depicting the overlaid Te and WSe2 lattices, highlighting both the true and approximate tiling. c) Atomic arrangement demonstrating the incommensurate moiré lattice, indicated by purple circles, superimposed on an 80x80 Angstroms simulated cell. d) Atomic configuration of the approximate tiling formed by overlaying the lattices, showcasing the expanded incommensurate moiré lattice. Te atoms are denoted in pink, Se in green, and W in gray.

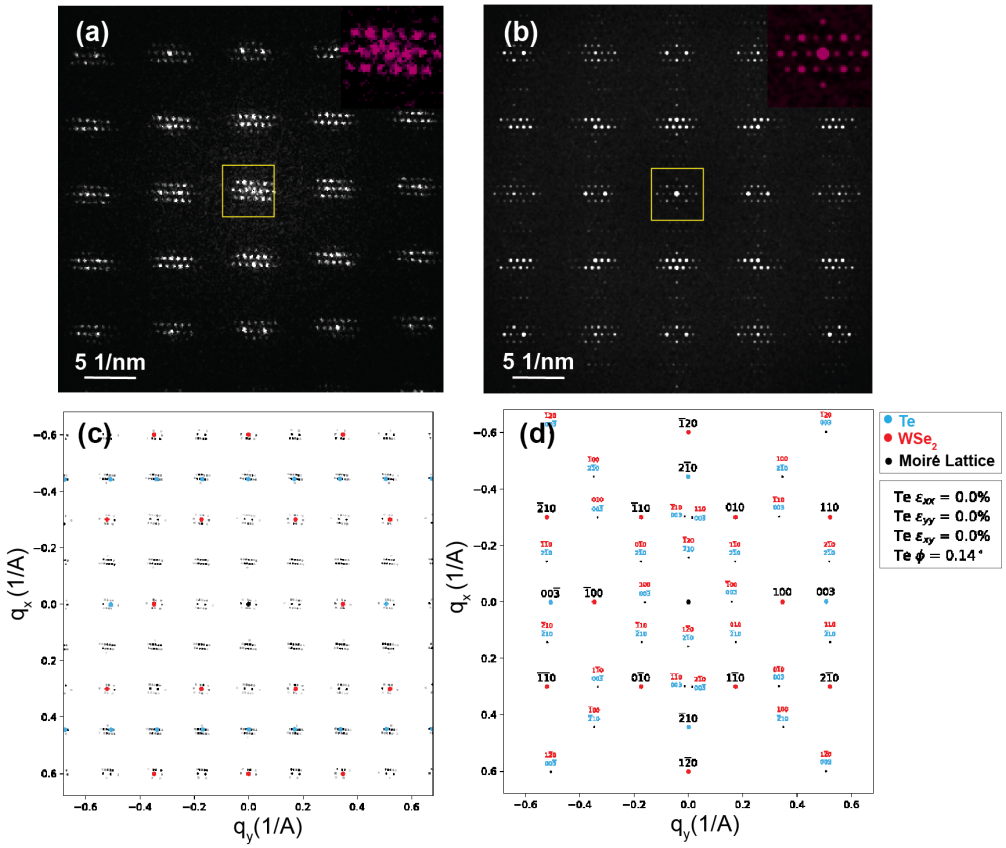


Figure 3.7: a) Fast Fourier Transform (FFT) of the high-resolution transmission electron microscopy (HRTEM) image shown in Figure 2f). The inset displays an enlarged view of the central region of the FFT. b) FFT of the simulated HRTEM image. c) Simulated reciprocal lattice demonstrating the impact of a 0.14-degree rotation tilt along the phi or z-axis on each "cluster" of peaks. d) Reciprocal lattice with labeled orientations of WSe2, Te, and moiré lattice peaks, as determined from the simulations

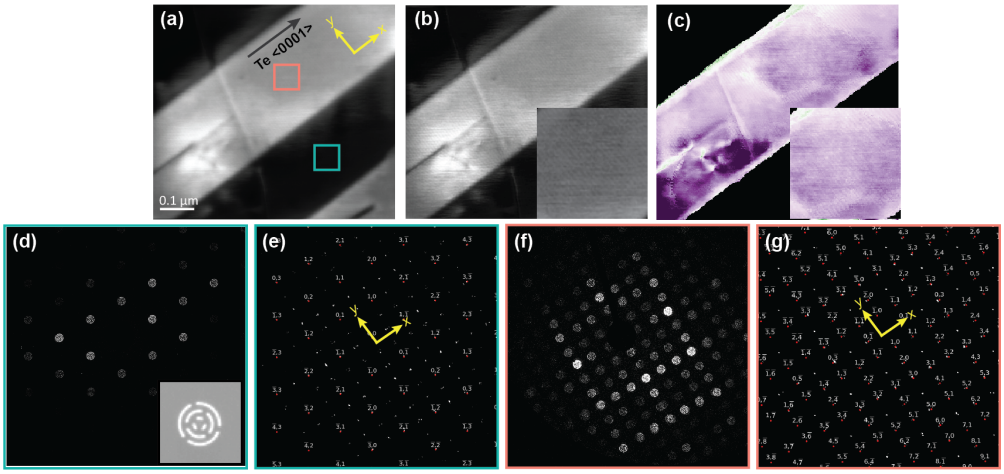


Figure 3.8: a)HAADAF image of the flake and the substrate. b) HAADAF image of the flake and the substrate. Inset of the moiré lattice on HAADAF image. c) Strain maps generated from Te lattice vectors. Inset of the moiré lattice on the strain map. d) The mean diffraction pattern of the 4DSTEM data. Bragg vector map (BVM) obtained from the e) $WSe_2$ and f) Te lattice vectors.

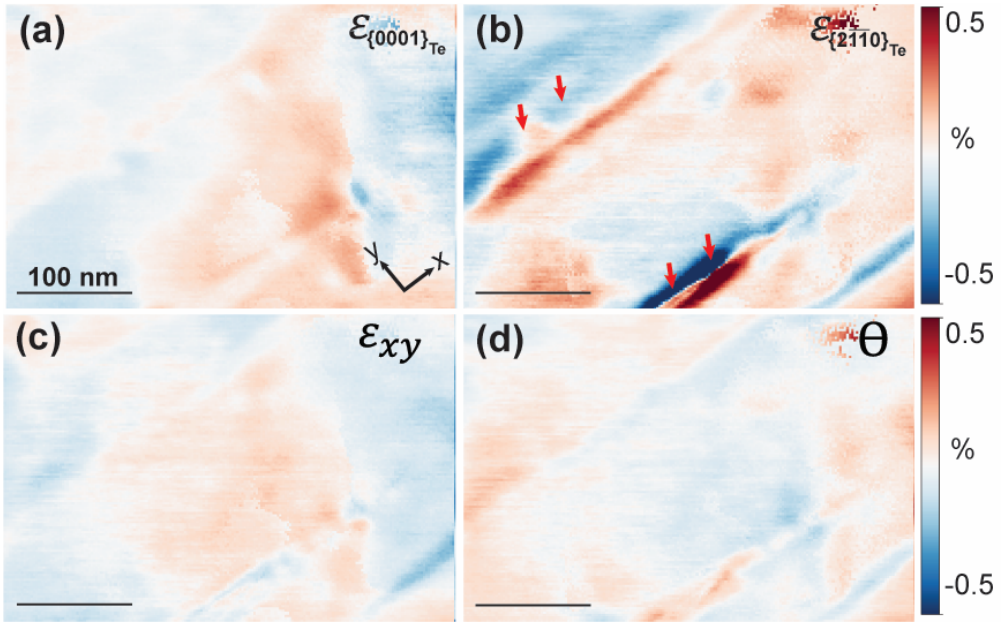


Figure 3.9: a-d) Strain maps generated using the $WSe_2$ lattice from different flakes. b) High tensile strains at the edges of the flakes are indicated by red arrows.

# Chapter 4

# Facile tensile testing platform for in-situ transmission electron microscopy of low-dimensional nanomaterials

The study delves into the challenges of implementing conventional tensile testing methodologies on thin films, particularly those placed on flexible substrates like polyimide or polydimethylsiloxane (PDMS). These substrates not only facilitate straining but also mitigate strain concentration issues found in free-standing films, distributing strain more uniformly. Such methods have demonstrated the ability to stretch metal films by up to 50% under tensile loads, showcasing their effectiveness in promoting uniform strain distribution.Preparing thin films for in-situ straining experiments in Transmission Electron Microscopy (TEM) demands precise control over film thickness, adhesion, stress induction during preparation, and the mitigation of strain localization and sample heating effects. This involves managing instrument limitations and controlling environmental factors. To address these challenges, a hybrid approach is proposed, wherein samples are deposited onto a flexible, electron-transparent substrate affixed to macroscopic copper sheets. This methodology, demonstrated through the examination of sputtered gold and transition metal dichalcogenide monolayers (TMDC) like $WS_2$ flakes, presents an alternative solution for the sample preparation for in-situ mechanical testing in TEM.

## 4.1 Introduction

The study of mechanical properties of materials has been a fundamental aspect of material science since its inception. These properties represent how crystalline systems respond to mechanical deformation, be it tension or compression, and are closely related to the system's elastic stiffness constants, such as the well-known bulk and shear modulus[104]. Detailed information about chemical bonding within a crystal and its relevant symmetry elements can be unveiled through careful examination of elastic strain, often depicted in a stress-strain curve[105]. However, most crystals can only endure moderate strains, contingent on their ductility, and the application of mechanical

strain in most cases leads to the emergence of crystal defects like dislocations and twins. These defects play a pivotal role in determining how a material responds to applied stress, and under high strains, they can trigger phase transitions and ultimately lead to fracture.

Tensile testing, a well-established scientific discipline, is employed to extract crucial information about various material properties, including the elastic modulus, Poisson ratio, yield strength, and fracture toughness[106]. Typically, test specimens are shaped like dogbones, concentrating stress at their narrowest cross-sectional point. As they elongate, structural changes occur in these high-stress regions, eventually resulting in fracture. However, for certain sample geometries, such as thin films, it is impractical to create macroscopic dogbone shapes, as the specimens would need to be microscopic yet large enough to be clamped within a tensile testing system.

Transmission electron microscopy (TEM) is the only method to directly visualize changes in a material's microstructure, including the formation of defects within a crystal lattice. The presence of a discontinuous deformation potential at these defects causes abrupt changes in diffraction conditions, providing contrast in high-resolution TEM images. Several studies have combined electron microscopy with tensile testing to examine phenomena like the formation of dislocation networks under tension compared to torsion [15, 107]. In-situ TEM measurements allow for the observation of dislocation motion under compressive strain using nano-pillar specimens and specialized TEM holders equipped with nano-indentation systems[108, 15, 109]. Advances in electron detectors and sources have made it possible to study these effects more closely, offering insights into how crystal defects propagate through a lattice and interact with other defects and grain boundaries[23].However, a significant challenge in these studies is sample preparation. Typical TEM specimens need to be less than approximately 100 nm in thickness for imaging, and existing in-situ straining platforms in TEM are not very versatile. One commonly used approach is the Gatan 654 straining platform, wherein a sample is first machined into the shape of a dog-bone (approximately 12 mm in length, 2 mm wide), and then mechanically polished in the central region for electron transparency [110]. The dog-bone is then clamped on both sides, where one end is connected to a finely geared DC motor, which provides a small elongation rate of approximately 1 µm/sec . This approach only works if the original crystal can be manufactured in relatively large sizes ( 12mm). Additionally, it must be possible to selectively thin the sample in a small area of the dog-bone [23].

Another approach is the use of MEMS (micro-electromechanical system) based push-to-pull design, as is the case with the Hysitron PI95 system, wherein a thin ($<$100nm) lamella is prepared in a focused ion beam (FIB) microscope, and then placed across a 2.5 µm wide gap in a silicon chip. Electron or ion beam induced deposition can be used to deposit platinum films, which serve to clamp the specimen on either side. The resulting samples can thus be strained in the TEM. Additionally, the presence of a force transducer on the indenter allows a simultaneous measurement of the stress across the lamella, hence yielding quantitative information about the stress-strain relationship[111].

In this study, we propose a hybrid approach. Samples are deposited on a flexible, electron-transparent substrate, which is then attached to macroscopic copper sheets using epoxy. These copper sheets serve as both stress concentrators and specimen carriers, which can be loaded into a Gatan 654 straining holder. The sample preparation process is similar to conventional TEM sample preparation, allowing for thin films to be spin-coated, sputter-coated, or transferred to the

flexible substrate through wet transfer. We prepared two samples: sputtered gold and transition metal dichalcogenide monolayers (TMDC),$WS_2$, flakes on TEM copper grids, and we transferred them onto copper sheets. This approach is reminiscent of what the thin-film community has used in the past when fabricating macroscopic samples for tensile testing. Thin foils were deposited onto polymeric substrates, such as kapton (polyimide) substrates, and the strain from the substrate was transferred to the thin film through van der Waals attract [17, 16]. With he help of electron microscopy, we are able to detect the structural changes in 2D materials,providing an ideal platform for strain engineering, enabling versatile modulation and significant enhancement of their optical properties.

## 4.2 Experimental Methods

### Preparation of Copper Sheets and Optical

### TEM sample preparation for Au/Pt film and TMDC flakes

We employed a Gatan Model 681 high-resolution ion beam coater operating at 9 keV beam energy and 300 µm current for a coating duration of 90 seconds to prepare sputtered gold (Au) sample.

$WS_2$ flakes were cleaved from a single crystal (SPI supplies) using Au-tape-assisted mechanical exfoliation on a 285 nm $SiO_2$/Si substrate [112]. These $WS_2$ flakes were finally put on the TEM grid using polystyrene assisted transfer technique as described below. We dissolved 13 grams of polystyrene (PS) particles with a molecular weight of 280,000 g/mol in 100 mL of toluene. Subsequently, we spin-coated the PS solution onto the $SiO_2$ substrate with $WS_2$ flakes at 2500 rpm for 60 seconds. The coated substrates were then baked on a hot plate at 60°C for 30 minutes. Following this, the PS coating on the substrates was trimmed according to the region of interest for $WS_2$ layer pickup before placing them in water. The detached polystyrene film with $WS_2$ flakes on the water surface was scooped onto the copper TEM grids (Lacey Formvar/Carbon, 200 mesh) following a bake at 80 °C for 50 min and soak into toluene to dissolve the PS.

### TEM data collection and analysis

We carried out in-situ straining experiments on sputtered Au film using a JEOL 3010 electron microscope, operating at an accelerating voltage of 200 kV. To facilitate these experiments, we loaded copper strips onto the Gatan 654 single tilt heating/straining holder, as depicted in Figure 1. Our experiments consisted of four steps, during which we applied a constant strain rate of 1 µm for 60 seconds.

Similarly, we conducted in-situ straining experiments on TMDC flakes utilizing the FEI Titan 60–300 microscope with a 200 kV acceleration voltage. After loading the TMDC flakes onto copper grids and mounting them on the copper strips, we applied tensional force to the $WS_2$, performing 10 elongation steps with 50 nm increments.

We employed the py4DSTEM package to generate radial integrated intensity profiles at various elongation stages. To ensure accuracy, we meticulously located the center of the diffraction pattern

and rectified any elliptical distortions, resulting in the creation of polar elliptical transformation images. Subsequently, we calculated radial Integral Intensity profiles by summing the images along the theta axis.

In our strain analysis using Diffraction Patterns (DPs), we begin by comparing them to a reference pattern acquired under similar, unstrained conditions, thereby establishing a relative measurement that negates the necessity of calibrating distortions resulting from projector lenses and detectors. Employing the py4DSTEM package, we identify Bragg discs. From these discs, we derive two distinct non-collinear two-dimensional vectors, denoted as g1 and g2, which together form the diffraction spot lattice of $WS_2$. These vectors, represented as

$$(gx1, gy1)$$

and

$$(gx2, gy2)$$

within a meticulously chosen two-dimensional framework, enable the construction of local diffraction matrices (G) corresponding to different diffraction patterns.

When $G_0$ represents the diffraction matrix of the reference area, we calculate the distortion matrix (D) at specific beam positions using the following equation (Equation 4.1):

$$D = (G_0 * G^{-}1)T \tag{4.1}$$

Here, the $'T'$ symbolizes matrix transposition. This distortion matrix can be further separated into two components: a rotation matrix (R) and a pure deformation matrix (F). The strain matrix (E) quantifies how the pure deformation matrix (F) differs from the identity matrix (I). This methodology enables us to extract four physically meaningful components from the deformation matrix $D$, encompassing three in-plane strain components $x, y, xy$ along with a rotation angle $\theta$.

## 4.3 Results and Discussion

In Figure 3.1, the placement of the TEM grid on the copper strip and the subsequent attachment to the Gatan 654 holder is depicted. Force is uniaxially applied in the $x$ -direction, as illustrated in Figure 3.1 (a) and (b). The TEM copper grid is securely attached to the copper strip using Crystalbond adhesive. First, we investigated the elongation of the TEM grid under an optical microscope, aiming to maintain the same location as elongation increased, as shown in Figure 3.1 (c)-(g). To quantify the applied strain, we measured the dimensions of the grid squares five times and calculated the mean of these measurements and the standard deviations. We generated two line plots to illustrate the changes in Dimension 1 and Dimension 2 at each elongation step, as depicted in Figure 3.1 (h) and (i). It is challenging to attach the TEM grid, as shown in Figure 3.1 (b), in a manner that exerts the force exactly parallel to the $x$ direction. Consequently, our findings deviate from Poisson's rule, which typically predicts that one of the dimensions should shrink while the other expands.

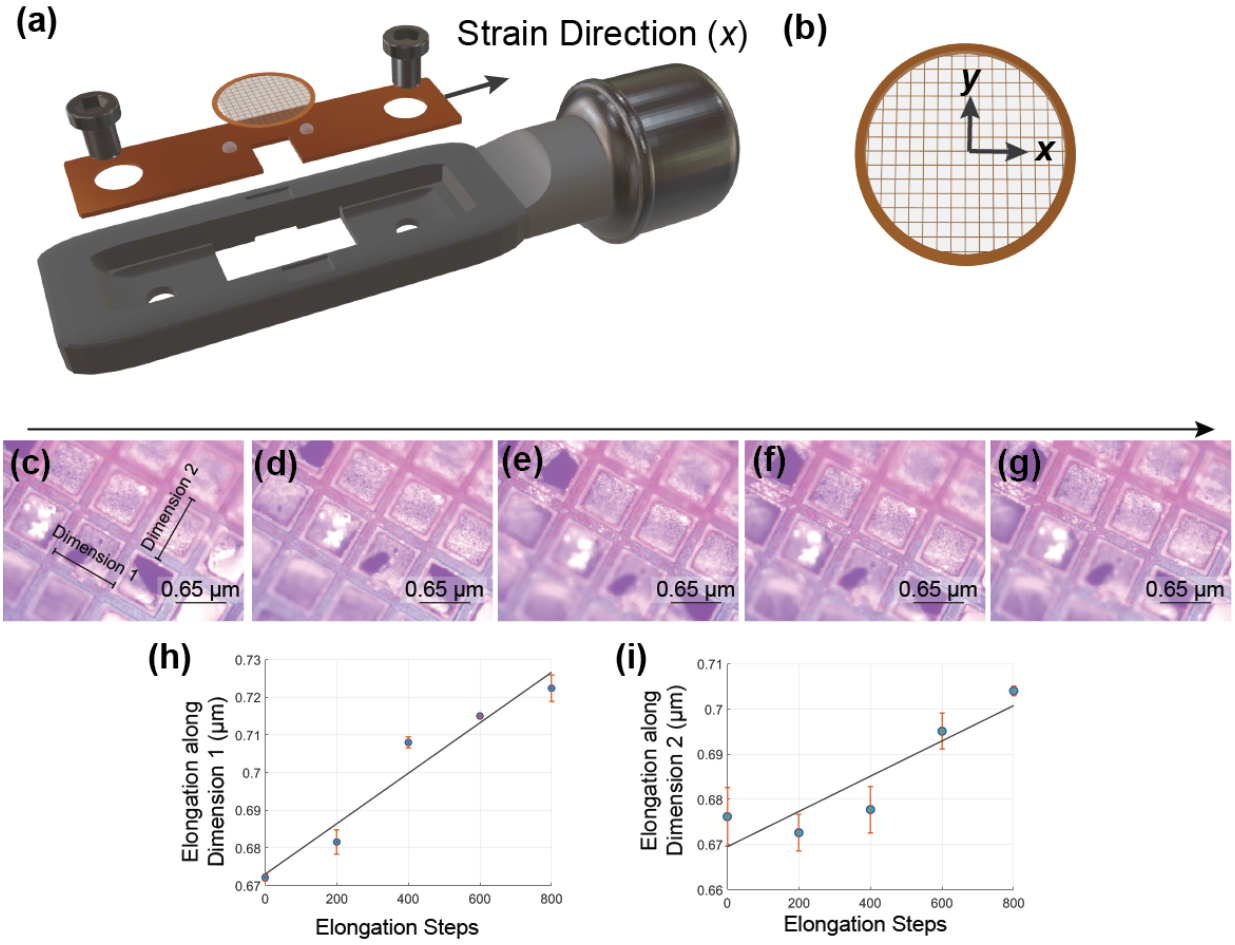


Figure 4.1: a) Shematic view of copper strip, TEM sample on Gatan straining holder. b) TEM grid showing the elongation direction. c-g) Optical microscope images under increasing elongation of the copper strip (left to right). h-i) 2D Plot showing the elongation at each steps calculated using Dimension 1 and Dimension 2.

After observing the elongation of the TEM grid under the uniaxial force applied to the copper strip with the assistance of an optical microscope, our next objective was to investigate the structural changes in the TEM. The initial sample on which we applied the method is sputtered gold. We elongated the sample and captured selected area diffraction (SAD) as well as bright field (BF) images at 30-second intervals. Figures 4.1 (a-d) depict bright field images of the gold at each step, while corresponding diffraction patterns are presented in Figures 4.1 (e-h). We demonstrated that our sample matched with the Au phase after carefully measuring the d-spacings, and we also presented the crystallographic planes on the diffraction pattern in Figure 4.1 (e). To quantify the strain applied to the samples, we plotted the radial integrated intensities of each diffraction pattern and illustrated the differences. As shown in Figure 4.1(i), the 1D plots shift to the left as the sample

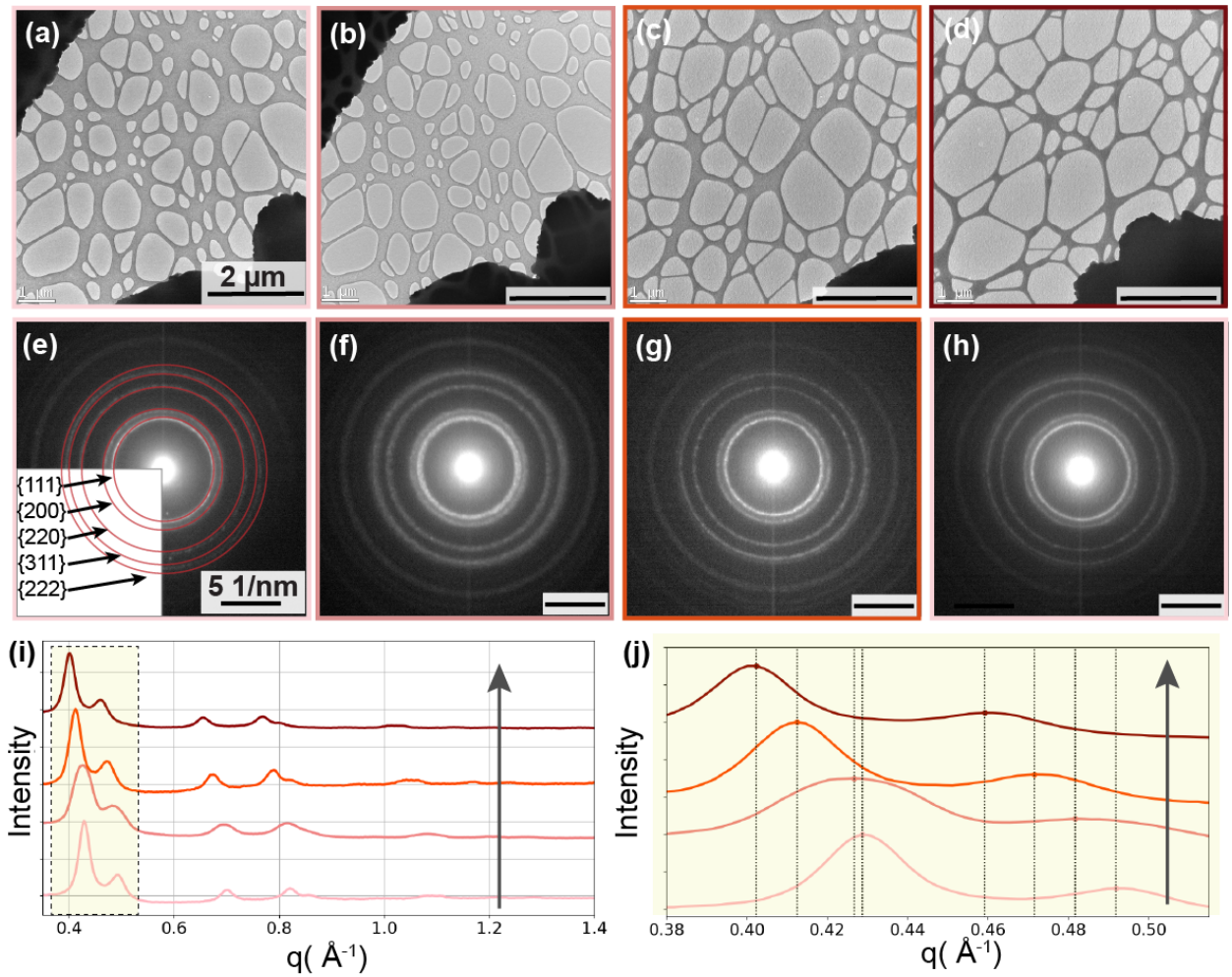


Figure 4.2: a-d) Bright field images under increasing elongation of the copper strip (left to right). e-h) SADP of the corresponding regions shown in (a-d. c) Radial profiles of the corresponding SADP in b. d) The zoomed in radial profiles around the dashed rectangle depicted in c. The direction of the arrows in c and d corresponds to the increasing elongation of the copper strip

elongates, indicating an increase in strain. Given that the plots are graphed against the reciprocal lattice vectors, this implies that the d-spacings corresponding to these positions increase as the strain intensifies. To enhance the visualization of the d-spacing increase, we highlighted the first two peaks in Figure 4.1 (j). We determined the peak locations by fitting Gaussian functions and represented the peak positions using vertical lines. We measured the total amount of strain relative to the initial strain and found it to be 6.5

We applied the same technique to a flexible TMDC semiconductor, $WS_2$, by incorporating 10 elongation steps, of which we displayed 5 in Figure 4.2. It is worth noting that, although we succeeded in transferring the TMDC onto the copper grid, we are aware of the potential bending

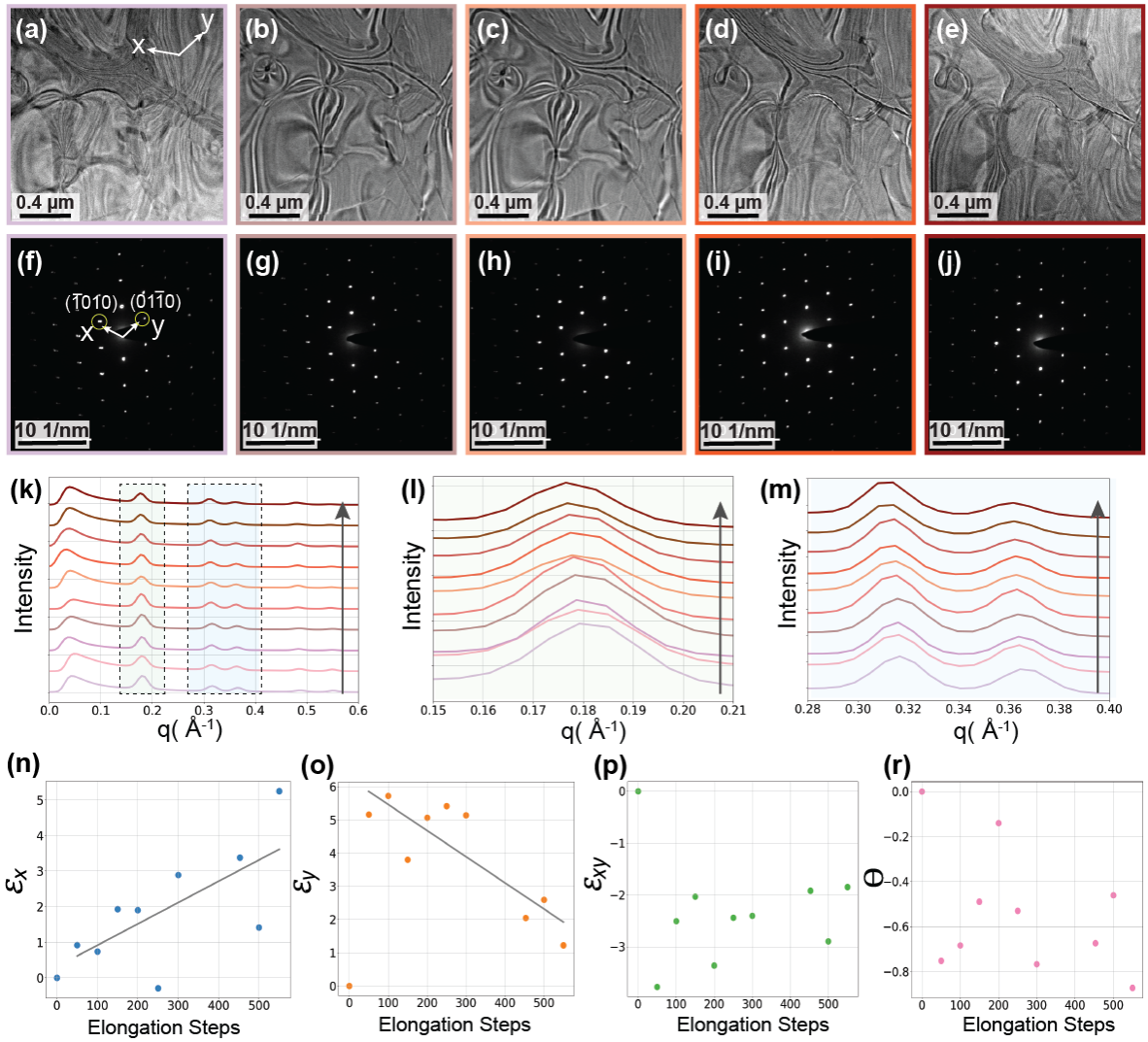


Figure 4.3: a-d) .Bright field images depict the progressive elongation of the copper strip from left to right (a-e). Corresponding SADPs are presented in (f-j), with radial profiles extracted from the SADP shown in (k). Zoomed-in radial profiles within the dashed rectangle in (k) are presented in (l-m). Arrows in (c and d) indicate the direction of increasing elongation of the copper strip. In-plane strain components, including $\varepsilon_x$, $\varepsilon_y$, $\varepsilon_{xy}$ and a rotation angle $\theta$, are shown in (n-r).

that may occur during the sample preparation. In Figure 2.4(k), we present the radial integrated intensity profiles of all the diffraction patterns. As indicated by the arrow, the elongation increases from the bottom to the top plot. To enhance the visibility of the differences, we have depicted the two main peaks in Figure 3 (l) and (m). We observed a leftward shift in the radial intensity plots from zero strain to a strain value of 550 µm, indicating lattice expansion. However, it's worth noting that this shift is not consistently observed in all steps due to the non-uniform nature of the strain.

As explained in the methodology section, we determined the positions of the peaks and identified the two lattice vectors that reconstruct the diffraction pattern. This is illustrated in Figure 4.3(f), where the x-axis corresponds to the $[1010]$ direction and the y-axis to the $[0110]$ direction. We extracted the in-plane strain components $\varepsilon_x$, $\varepsilon_y$, and shear using the two main vectors $(x, y)$. We observed an opposite trend in the strain along the x and y directions but found no evidence of shear or rotation. The anisotropic crystal structure inherent to $WS_2$ results in disparate reactions to applied strain along distinct axes, leading to an expansion along one axis and a compression along another. It is worth to note that according to theoretical calculations, an ultralarge elastic strain more than 20% along armchair and 10% along the zigzag direction can be achieved in ideal single crystalline monolayer $WS_2$ [113]. Therefore, it shows a great potential to tailor their physical and chemical properties toward novel functional device applications.

## 4.4 Conclusions

Traditional tensile testing has long been a cornerstone for extracting essential material properties, yet it faces practical constraints, especially when applied to unconventional sample geometries like thin films. To address these limitations, we introduced an innovative hybrid approach, combining the capabilities of transmission electron microscopy (TEM) with flexible substrates and macroscopic copper sheets, allowing for the in-depth examination of materials under mechanical strain.

We observed, with precision, the elongation of TEM grid samples under uniaxial force, enabled by the methodology involving the use of TEM copper grids and copper sheets. This approach simplified sample preparation and broadened our capacity to explore the mechanical properties of materials at the nanoscale. The data we collected revealed striking insights into the mechanical responses of various materials, notably the sputtered gold (Au) and transition metal dichalcogenide (TMDC), specifically $WS_2$. Examining structural alterations through in-situ mechanical testing within TEM addresses limitations inherent in ex-situ methodologies, providing crucial insights derived from real-time observations.

For sputtered Au, we meticulously tracked structural changes, demonstrating the shifting d-spacings and changes in diffraction patterns as the material experienced strain. Through careful analysis, we determined the total amount of strain relative to the initial state, quantifying a 6.5 % increase in strain. In the case of TMDC, specifically WS2, our methodology allowed us to investigate the impact of strain on the crystal lattice. The strain analysis of WS2 revealed non-uniform strain distribution, demonstrating the anisotropic nature of the crystal structure, leading to both expansion and compression along different axes. These findings, when combined with theoretical predictions of ultralarge elastic strain in $WS_2$, hold great promise for tailoring its physical and chemical properties for advanced device applications.

In summary, our study not only introduced a hybrid approach for studying mechanical properties but also generated valuable insights into the mechanical behavior of different materials at the nanoscale. These findings open exciting avenues for further research and applications in the in-situ straining experiments. Before publishing our paper, our ultimate objective is to incorporate the computational results obtained through the finite element method (FEM). These results will

serve to illustrate the local strain fields, the impact of TEM grid rotation on the strain fields, and the positioning of TMDC flakes in relation to elongations.

# Chapter 5

# Conclusions and future work

Throughout our research, we have uncovered significant insights and made substantial advancements in the realm of materials science. Our investigations have primarily centered on tellurium and selenium chalcogens, as well as transition metal dichalcogenides (TMDCs).

In chapter 2, we have thoroughly explored the short- to medium-range ordering in amorphous Te-Se thin films, employing a combination of experimental studies and advanced atomic simulations. This work has not only deepened our understanding of these materials but has also shed light on their stability and behaviors, attributing variations in bond character to the evolving medium-range order populations with different selenium (Se) content.

In chapter 3, we've made observations regarding the formation of moiré lattices resulting from the interactions between tellurium crystalline films and transition metal dichalcogenides (TMDs). These moiré structures exhibit spatial variations, contributing to intriguing properties such as superconductivity, topological conducting channels, and advanced optoelectronic behaviors [10, 114]. We achieved to show the exact orientation relationship between the heterostuctures with the help of CoM-DPC and image simulations. This study can be extended to compare the structure-property relationship by combining Electron Energy Loss Spectroscopy (EELS) and scanning nanodiffraction techniques. For instance, in a recent paper, high-resolution scanning transmission electron microscopy (STEM) and electron energy-loss spectroscopy (EELS) were employed to investigate the effect of the twist angle in $MoS_2$/$WSe_2$ heterostructures. It was found that the optical response of the heterostructure varies within the moiré supercell, exhibiting a lower energy absorption peak in regions characterized by AA stacking [115]. In the light of this we expect c change in the optical responses of the substrate and the film after the formation of the heterostructure.

In Chapter 4, we introduced an approach combining transmission electron microscopy (TEM) with TEM copper grids and copper sheets, revealing valuable insights into mechanical properties at the nanoscale. This approach enabled precise measurements of strain in materials like sputtered gold (Au), quantifying a 6.5% increase in strain, and WS2, which exhibited non-uniform strain distribution. These findings, along with theoretical predictions of ultralarge elastic strain in WS2, emphasize the significance of our findings in advancing in-situ straining experiments.

# Bibliography


[1] Ersan Y. Muslih, Badrul Munir, and Mohammad Mansoob Khan. "Advances in chalcogenides and chalcogenides-based nanomaterials such as sulfides, selenides, and tellurides". en. In: *Chalcogenide-Based Nanomaterials as Photocatalysts*. Elsevier, 2021, pp. 7–31. ISBN: 978-0-12-820498-6. DOI: 10.1016/B978-0-12-820498-6.00002-0. URL: https://linkinghub.elsevier.com/retrieve/pii/B9780128204986000020 (visited on 10/03/2023).

[2] Aday J. Molina-Mendoza et al. "Electronic Bandgap and Exciton Binding Energy of Layered Semiconductor $TiS_3$". en. In: *Advanced Electronic Materials* 1.9 (Sept. 2015). ISSN: 2199160X. DOI: 10.1002/aelm.201500126. URL: https://onlinelibrary.wiley.com/doi/10.1002/aelm.201500126 (visited on 02/28/2022).

[3] Bruno Bureau et al. "Selenium-Tellurium Sequences in Binary Glasses as Depicted by $^{77}$Se and $^{125}$Te NMR". en. In: *The Journal of Physical Chemistry B* 109.13 (Apr. 2005), pp. 6130–6135. ISSN: 1520-6106, 1520-5207. DOI: 10.1021/jp044398n. URL: https://pubs.acs.org/doi/10.1021/jp044398n (visited on 06/16/2022).

[4] Pierre Lucas et al. "Telluride glasses for far infrared photonic applications". en. In: *Optical Materials Express* 3.8 (Aug. 2013), p. 1049. ISSN: 2159-3930. DOI: 10.1364/OME.3.001049. URL: https://opg.optica.org/ome/abstract.cfm?uri=ome-3-8-1049 (visited on 06/16/2022).

[5] L. Q. Xing et al. "Relation between short-range order and crystallization behavior in Zr-based amorphous alloys". en. In: *Applied Physics Letters* 77.13 (Sept. 2000), pp. 1970–1972. ISSN: 0003-6951, 1077-3118. DOI: 10.1063/1.1313255. URL: https://pubs.aip.org/apl/article/77/13/1970/112593/Relation-between-short-range-order-and (visited on 10/03/2023).

[6] Elisabeth Bianco et al. "Large-area ultrathin Te films with substrate-tunable orientation". en. In: *Nanoscale* 12.23 (2020), pp. 12613–12622. ISSN: 2040-3364, 2040-3372. DOI: 10.1039/D0NR01251C. URL: http://xlink.rsc.org/?DOI=D0NR01251C (visited on 09/28/2020).

[7] Xiaochun Huang et al. "Epitaxial Growth and Band Structure of Te Film on Graphene". en. In: *Nano Letters* 17.8 (Aug. 2017), pp. 4619–4623. ISSN: 1530-6984, 1530-6992. DOI: 10.1021/acs.nanolett.7b01029. URL: https://pubs.acs.org/doi/10.1021/acs.nanolett.7b01029 (visited on 08/23/2023).

[8] Yixiu Wang et al. "Field-effect transistors made from solution-grown two-dimensional tellurene". en. In: *Nature Electronics* 1.4 (Apr. 2018), pp. 228–236. ISSN: 2520-1131. DOI: 10.1038/s41928-018-0058-4. URL: https://www.nature.com/articles/s41928-018-0058-4 (visited on 10/03/2023).

[9] Chunsong Zhao et al. "Orientated Growth of Ultrathin Tellurium by van der Waals Epitaxy". en. In: *Advanced Materials Interfaces* 9.5 (Feb. 2022), p. 2101540. ISSN: 2196-7350, 2196-7350. DOI: 10.1002/admi.202101540. URL: https://onlinelibrary.wiley.com/doi/10.1002/admi.202101540 (visited on 05/01/2022).

[10] Feng He et al. "Moiré Patterns in 2D Materials: A Review". en. In: *ACS Nano* 15.4 (Apr. 2021), pp. 5944–5958. ISSN: 1936-0851, 1936-086X. DOI: 10.1021/acsnano.0c10435. URL: https://pubs.acs.org/doi/10.1021/acsnano.0c10435 (visited on 12/21/2022).

[11] Dinkar Nandwana and Elif Ertekin. "Ripples, Strain, and Misfit Dislocations: Structure of Graphene–Boron Nitride Superlattice Interfaces". en. In: *Nano Letters* 15.3 (Mar. 2015), pp. 1468–1475. ISSN: 1530-6984, 1530-6992. DOI: 10.1021/nl505005t. URL: https://pubs.acs.org/doi/10.1021/nl505005t (visited on 08/18/2021).

[12] Hemant Kumar, Liang Dong, and Vivek B. Shenoy. "Limits of Coherency and Strain Transfer in Flexible 2D van der Waals Heterostructures: Formation of Strain Solitons and Interlayer Debonding". en. In: *Scientific Reports* 6.1 (Dec. 2016), p. 21516. ISSN: 2045-2322. DOI: 10.1038/srep21516. URL: http://www.nature.com/articles/srep21516 (visited on 12/01/2022).

[13] Heng Zhang et al. "Strain Relaxation in "2D/2D and 2D/3D Systems": Highly Textured Mica/$Bi_2Te_3$, $Sb_2Te_3$/$Bi_2Te_3$, and $Bi_2Te_3$/GeTe Heterostructures". en. In: *ACS Nano* 15.2 (Feb. 2021), pp. 2869–2879. ISSN: 1936-0851, 1936-086X. DOI: 10.1021/acsnano.0c08842. URL: https://pubs.acs.org/doi/10.1021/acsnano.0c08842 (visited on 05/16/2022).

[14] M.A. Meyers, O. Vöhringer, and V.A. Lubarda. "The onset of twinning in metals: a constitutive description". en. In: *Acta Materialia* 49.19 (Nov. 2001), pp. 4025–4039. ISSN: 13596454. DOI: 10.1016/S1359-6454(01)00300-7. URL: https://linkinghub.elsevier.com/retrieve/pii/S1359645401003007 (visited on 10/19/2023).

[15] Jeff T. M. De Hosson et al. "In situ TEM nanoindentation and dislocation-grain boundary interactions: a tribute to David Brandon". en. In: *Journal of Materials Science* 41.23 (Dec. 2006), pp. 7704–7719. ISSN: 0022-2461, 1573-4803. DOI: 10.1007/s10853-006-0472-2. URL: http://link.springer.com/10.1007/s10853-006-0472-2 (visited on 10/19/2023).

[16] Yong Xiang et al. "High ductility of a metal film adherent on a polymer substrate". en. In: *Applied Physics Letters* 87.16 (Oct. 2005), p. 161910. ISSN: 0003-6951, 1077-3118. DOI: 10.1063/1.2108110. URL: https://pubs.aip.org/apl/article/87/16/161910/909972/High-ductility-of-a-metal-film-adherent-on-a (visited on 11/16/2023).

[17] Iris Niehues et al. “Interlayer excitons in bilayer MoS $_2$ under uniaxial tensile strain”. en. In: *Nanoscale* 11.27 (2019), pp. 12788–12792. ISSN: 2040-3364, 2040-3372. DOI: 10.1039/C9NR03332G. URL: http://xlink.rsc.org/?DOI=C9NR03332G (visited on 11/16/2023).

[18] David B. Williams and C. Barry Carter. *Transmission electron microscopy: a textbook for materials science*. en. 2nd ed. New York: Springer, 2008. ISBN: 978-0-387-76500-6.

[19] Colin Ophus. “Four-Dimensional Scanning Transmission Electron Microscopy (4D-STEM): From Scanning Nanodiffraction to Ptychography and Beyond”. en. In: *Microscopy and Microanalysis* 25.3 (June 2019), pp. 563–582. ISSN: 1431-9276, 1435-8115. DOI: 10.1017/S1431927619000497. URL: https://www.cambridge.org/core/product/identifier/S1431927619000497/type/journal_article (visited on 08/26/2022).

[20] Benjamin H. Savitzky et al. “py4DSTEM: A Software Package for Four-Dimensional Scanning Transmission Electron Microscopy Data Analysis”. en. In: *Microscopy and Microanalysis* 27.4 (Aug. 2021), pp. 712–743. ISSN: 1431-9276, 1435-8115. DOI: 10.1017/S1431927621000477. URL: https://academic.oup.com/mam/article/27/4/712/6888063 (visited on 10/18/2023).

[21] Philipp M. Pelz et al. “Real-time interactive 4D-STEM phase-contrast imaging from electron event representation data”. en. In: *Microscopy and Microanalysis* 27.S1 (Aug. 2021). arXiv:2104.06336 [cond-mat, physics:physics], pp. 188–189. ISSN: 1431-9276, 1435-8115. DOI: 10.1017/S1431927621001288. URL: http://arxiv.org/abs/2104.06336 (visited on 09/27/2022).

[22] Colin Ophus et al. “Automated Crystal Orientation Mapping in py4DSTEM using Sparse Correlation Matching”. en. In: *Microscopy and Microanalysis* 28.2 (Apr. 2022), pp. 390–403. ISSN: 1431-9276, 1435-8115. DOI: 10.1017/S1431927622000101. URL: https://academic.oup.com/mam/article/28/2/390/6889402 (visited on 03/28/2023).

[23] Thomas C. Pekin et al. “In situ nanobeam electron diffraction strain mapping of planar slip in stainless steel”. en. In: *Scripta Materialia* 146 (Mar. 2018), pp. 87–90. ISSN: 13596462. DOI: 10.1016/j.scriptamat.2017.11.005. URL: https://linkinghub.elsevier.com/retrieve/pii/S1359646217306462 (visited on 04/30/2022).

[24] Paul M. Voyles and John R. Abelson. “Medium-range order in amorphous silicon measured by fluctuation electron microscopy”. en. In: *Solar Energy Materials and Solar Cells* 78.1-4 (July 2003), pp. 85–113. ISSN: 09270248. DOI: 10.1016/S0927-0248(02)00434-8. URL: https://linkinghub.elsevier.com/retrieve/pii/S0927024802004348 (visited on 01/26/2022).

[25] J. D. Bernal. “Geometry of the Structure of Monatomic Liquids”. en. In: *Nature* 185.4706 (Jan. 1960), pp. 68–70. ISSN: 0028-0836, 1476-4687. DOI: 10.1038/185068a0. URL: https://www.nature.com/articles/185068a0 (visited on 03/30/2023).

[26] I. Lobato and D. Van Dyck. "An accurate parameterization for scattering factors, electron densities and electrostatic potentials for neutral atoms that obey all physical constraints". en. In: *Acta Crystallographica Section A Foundations and Advances* 70.6 (Nov. 2014), pp. 636–649. ISSN: 2053-2733. DOI: 10.1107/S205327331401643X. URL: http://scripts.iucr.org/cgi-bin/paper?S205327331401643X (visited on 06/26/2021).

[27] Štefan Michalik et al. "Short range order and crystallization of Cu–Hf metallic glasses". en. In: *Journal of Alloys and Compounds* 853 (Feb. 2021), p. 156775. ISSN: 09258388. DOI: 10.1016/j.jallcom.2020.156775. URL: https://linkinghub.elsevier.com/retrieve/pii/S092583882033139X (visited on 11/19/2021).

[28] T. Ichikawa. "Electron Diffraction Study of the Local Atomic Arrangement in Amorphous Tellurium Films: Electron Diffraction Study of the Local Atomic Arrangement in Te". en. In: *physica status solidi (b)* 56.2 (Apr. 1973), pp. 707–715. ISSN: 03701972. DOI: 10.1002/pssb.2220560235. URL: http://doi.wiley.com/10.1002/pssb.2220560235 (visited on 10/07/2020).

[29] R. Bellissent and G. Tourand. "Short range order in amorphous and liquid Se1-xTex systems". en. In: *Journal of Non-Crystalline Solids* 35-36 (Jan. 1980), pp. 1221–1226. ISSN: 00223093. DOI: 10.1016/0022-3093(80)90364-6. URL: https://linkinghub.elsevier.com/retrieve/pii/0022309380903646 (visited on 10/07/2020).

[30] Badri Shyam et al. "Measurement and Modeling of Short and Medium Range Order in Amorphous Ta2O5 Thin Films". en. In: *Scientific Reports* 6.1 (Oct. 2016), p. 32170. ISSN: 2045-2322. DOI: 10.1038/srep32170. URL: http://www.nature.com/articles/srep32170 (visited on 11/13/2020).

[31] David J.H. Cockayne. "The Study of Nanovolumes of Amorphous Materials Using Electron Scattering". en. In: *Annual Review of Materials Research* 37.1 (Aug. 2007), pp. 159–187. ISSN: 1531-7331, 1545-4118. DOI: 10.1146/annurev.matsci.35.082803.103337. URL: http://www.annualreviews.org/doi/10.1146/annurev.matsci.35.082803.103337 (visited on 09/29/2021).

[32] K Tamura et al. "EXAFS measurements of liquid Se-Te mixtures". en. In: *Journal of Physics: Condensed Matter* 3.38 (Sept. 1991), pp. 7495–7510. ISSN: 0953-8984, 1361-648X. DOI: 10.1088/0953-8984/3/38/021. URL: https://iopscience.iop.org/article/10.1088/0953-8984/3/38/021 (visited on 06/03/2021).

[33] Vuk Uskoković. "X-ray photoelectron and ion scattering spectroscopic surface analyses of amorphous and crystalline calcium phosphate nanoparticles with different chemical histories". en. In: *Physical Chemistry Chemical Physics* 22.10 (2020), pp. 5531–5547. ISSN: 1463-9076, 1463-9084. DOI: 10.1039/C9CP06529F. URL: http://xlink.rsc.org/?DOI=C9CP06529F (visited on 11/16/2023).

[34] B. Günther and O. Kanert. "Nuclear-magnetic-resonance study of crystalline tellurium and selenium". en. In: *Physical Review B* 31.1 (Jan. 1985), pp. 20–33. ISSN: 0163-1829. DOI: 10.1103/PhysRevB.31.20. URL: https://link.aps.org/doi/10.1103/PhysRevB.31.20 (visited on 10/21/2021).

[35] T.L. Daulton, K.S. Bondi, and K.F. Kelton. "Nanobeam diffraction fluctuation electron microscopy technique for structural characterization of disordered materials—Application to Al88-xY7Fe5Tix metallic glasses". en. In: *Ultramicroscopy* 110.10 (Sept. 2010), pp. 1279–1289. ISSN: 03043991. DOI: 10.1016/j.ultramic.2010.05.010. URL: https://linkinghub.elsevier.com/retrieve/pii/S030439911000166X (visited on 01/11/2022).

[36] M. M. J. Treacy and J. M. Gibson. "Variable Coherence Microscopy: a Rich Source of Structural Information from Disordered Materials". en. In: *Acta Crystallographica Section A Foundations of Crystallography* 52.2 (Mar. 1996), pp. 212–220. ISSN: 01087673. DOI: 10.1107/S0108767395012876. URL: http://scripts.iucr.org/cgi-bin/paper?S0108767395012876 (visited on 01/11/2022).

[37] Bong-Sub Lee, Stephen G. Bishop, and John R. Abelson. "Fluctuation Transmission Electron Microscopy: Detecting Nanoscale Order in Disordered Structures". en. In: *Chemistry Europe* 11.11 (July 2010), pp. 2311–2317. ISSN: 14394235, 14397641. DOI: 10.1002/cphc.201000153. URL: http://doi.wiley.com/10.1002/cphc.201000153 (visited on 07/17/2020).

[38] Tian T. Li, Kristof Darmawikarta, and John R. Abelson. "Quantifying nanoscale order in amorphous materials via scattering covariance in fluctuation electron microscopy". en. In: *Ultramicroscopy* 133 (Oct. 2013), pp. 95–100. ISSN: 03043991. DOI: 10.1016/j.ultramic.2013.06.017. URL: https://linkinghub.elsevier.com/retrieve/pii/S0304399113001605 (visited on 07/10/2020).

[39] Bengisu Sari et al. "Structural heterogeneity in non-crystalline Te $_x$ Se1-x thin films". en. In: *Applied Physics Letters* 121.1 (July 2022), p. 012101. ISSN: 0003-6951, 1077-3118. DOI: 10.1063/5.0094600. URL: https://aip.scitation.org/doi/10.1063/5.0094600 (visited on 10/31/2022).

[40] José Marcial and John McCloy. "Role of short range order on crystallization of tectosilicate glasses: A diffraction study". en. In: *Journal of Non-Crystalline Solids* 505 (Feb. 2019), pp. 131–143. ISSN: 00223093. DOI: 10.1016/j.jnoncrysol.2018.10.050. URL: https://linkinghub.elsevier.com/retrieve/pii/S0022309318306422 (visited on 11/19/2021).

[41] Thomas C. Pekin et al. "Direct measurement of nanostructural change during in situ deformation of a bulk metallic glass". en. In: *Nature Communications* 10.1 (Dec. 2019), p. 2445. ISSN: 2041-1723. DOI: 10.1038/s41467-019-10416-5. URL: http://www.nature.com/articles/s41467-019-10416-5 (visited on 10/20/2020).

[42] Soohyun Im et al. “Direct determination of structural heterogeneity in metallic glasses using four-dimensional scanning transmission electron microscopy”. en. In: *Ultramicroscopy* 195 (Dec. 2018), pp. 189–193. ISSN: 03043991. DOI: 10.1016/j.ultramic.2018.09.005. URL: https://linkinghub.elsevier.com/retrieve/pii/S030439911830158X (visited on 09/17/2020).

[43] W.G. Stratton and P.M. Voyles. “A phenomenological model of fluctuation electron microscopy for a nanocrystal/amorphous composite”. en. In: *Ultramicroscopy* 108.8 (July 2008), pp. 727–736. ISSN: 03043991. DOI: 10.1016/j.ultramic.2007.11.004. URL: https://linkinghub.elsevier.com/retrieve/pii/S0304399107002549 (visited on 09/29/2021).

[44] Aram Rezikyan et al. “Speckle Suppression by Decoherence in Fluctuation Electron Microscopy”. en. In: *Microscopy and Microanalysis* 21.6 (Dec. 2015), pp. 1455–1474. ISSN: 1431-9276, 1435-8115. DOI: 10.1017/S1431927615015135. URL: https://www.cambridge.org/core/product/identifier/S1431927615015135/type/journal_article (visited on 02/28/2022).

[45] Paul. A. Vermeulen, Jamo Momand, and Bart J. Kooi. “Reversible amorphous-crystalline phase changes in a wide range of Se $_{1-x}$ Te $_{x}$ alloys studied using ultrafast differential scanning calorimetry”. en. In: *The Journal of Chemical Physics* 141.2 (July 2014), p. 024502. ISSN: 0021-9606, 1089-7690. DOI: 10.1063/1.4886185. URL: http://aip.scitation.org/doi/10.1063/1.4886185 (visited on 01/11/2022).

[46] Bing Yuan et al. “Chemical order in binary Se-Te glasses: Results from high-resolution 2D 77Se and 125Te MATPASS NMR spectroscopy”. en. In: *Journal of Non-Crystalline Solids* 544 (Sept. 2020), p. 120212. ISSN: 00223093. DOI: 10.1016/j.jnoncrysol.2020.120212. (Visited on 10/21/2021).

[47] Robert Bellissent. “Short range order in the disordered states of selenium-tellurium mixtures”. en. In: *Nuclear Instruments and Methods in Physics Research* 199.1-2 (Aug. 1982), pp. 289–294. ISSN: 01675087. DOI: 10.1016/0167-5087(82)90218-6. URL: https://linkinghub.elsevier.com/retrieve/pii/0167508782902186 (visited on 12/11/2023).

[48] H Thurn and J Ruska. “SHOWN BY DENSITY MEASUREMENTS”. en. In: (), p. 13.

[49] Keiji Itoh. “Structure of Se-Te glasses studied using neutron, X-ray diffraction and reverse Monte Carlo modelling”. en. In: *Journal of Solid State Chemistry* 246 (Feb. 2017), pp. 372–378. ISSN: 00224596. DOI: 10.1016/j.jssc.2016.12.012. URL: https://linkinghub.elsevier.com/retrieve/pii/S0022459616304881 (visited on 10/02/2023).

[50] M. Majid et al. “XAFS study of interchain and intrachain order in Se 1 - x Te x glasses: Nearest neighbors”. en. In: *Physical Review B* 58.10 (Sept. 1998), pp. 6104–6114. ISSN: 0163-1829, 1095-3795. DOI: 10.1103/PhysRevB.58.6104. URL: https://link.aps.org/doi/10.1103/PhysRevB.58.6104 (visited on 02/28/2022).

[51] Andrey Tverjanovich et al. "Structure of Se-Te glasses by Raman spectroscopy and DFT modeling". en. In: *Journal of the American Ceramic Society* 101.11 (Nov. 2018), pp. 5188–5197. ISSN: 00027820. DOI: 10.1111/jace.15758. URL: https://onlinelibrary.wiley.com/doi/10.1111/jace.15758 (visited on 03/04/2023).

[52] E. Grison. "Studies on Tellurium-Selenium Alloys". en. In: *The Journal of Chemical Physics* 19.9 (Sept. 1951), pp. 1109–1113. ISSN: 0021-9606, 1089-7690. DOI: 10.1063/1.1748484. URL: http://aip.scitation.org/doi/10.1063/1.1748484 (visited on 07/23/2020).

[53] Xiaoke Mu et al. "Radial distribution function imaging by STEM diffraction: a method development in resolving the mysteries of amorphous materials". en. In: *European Microscopy Congress 2016: Proceedings*. Ed. by European Microscopy Society. Weinheim, Germany: Wiley-VCH Verlag GmbH & Co. KGaA, Dec. 2016, pp. 617–618. ISBN: 978-3-527-80846-5. DOI: 10.1002/9783527808465.EMC2016.5718. URL: https://onlinelibrary.wiley.com/doi/10.1002/9783527808465.EMC2016.5718 (visited on 03/04/2023).

[54] G. Kresse and J. Hafner. "*Ab initio* molecular dynamics for liquid metals". en. In: *Physical Review B* 47.1 (Jan. 1993), pp. 558–561. ISSN: 0163-1829, 1095-3795. DOI: 10.1103/PhysRevB.47.558. URL: https://link.aps.org/doi/10.1103/PhysRevB.47.558 (visited on 03/04/2023).

[55] G. Kresse and J. Furthmüller. "Efficiency of ab-initio total energy calculations for metals and semiconductors using a plane-wave basis set". en. In: *Computational Materials Science* 6.1 (July 1996), pp. 15–50. ISSN: 09270256. DOI: 10.1016/0927-0256(96)00008-0. URL: https://linkinghub.elsevier.com/retrieve/pii/0927025696000080 (visited on 03/04/2023).

[56] G. Kresse and J. Furthmüller. "Efficient iterative schemes for *ab initio* total-energy calculations using a plane-wave basis set". en. In: *Physical Review B* 54.16 (Oct. 1996), pp. 11169–11186. ISSN: 0163-1829, 1095-3795. DOI: 10.1103/PhysRevB.54.11169. URL: https://link.aps.org/doi/10.1103/PhysRevB.54.11169 (visited on 03/04/2023).

[57] P. E. Blöchl. "Projector augmented-wave method". en. In: *Physical Review B* 50.24 (Dec. 1994), pp. 17953–17979. ISSN: 0163-1829, 1095-3795. DOI: 10.1103/PhysRevB.50.17953. URL: https://link.aps.org/doi/10.1103/PhysRevB.50.17953 (visited on 03/04/2023).

[58] John P. Perdew, Kieron Burke, and Matthias Ernzerhof. "Generalized Gradient Approximation Made Simple". en. In: *Physical Review Letters* 77.18 (Oct. 1996), pp. 3865–3868. ISSN: 0031-9007, 1079-7114. DOI: 10.1103/PhysRevLett.77.3865. URL: https://link.aps.org/doi/10.1103/PhysRevLett.77.3865 (visited on 03/04/2023).

[59] M. Parrinello and A. Rahman. "Crystal Structure and Pair Potentials: A Molecular Dynamics Study". en. In: *Physical Review Letters* 45.14 (Oct. 1980), pp. 1196–1199. ISSN: 0031-9007. DOI: 10.1103/PhysRevLett.45.1196. URL: https://link.aps.org/doi/10.1103/PhysRevLett.45.1196 (visited on 03/04/2023).

[60] Ralf Brüning, Edward Irving, and Gilles LeBlanc. "Reverse Monte Carlo study of structural relaxation in vitreous selenium". en. In: *Journal of Applied Physics* 89.6 (Mar. 2001), pp. 3215–3222. ISSN: 0021-8979, 1089-7550. DOI: 10.1063/1.1350412. URL: http://aip.scitation.org/doi/10.1063/1.1350412 (visited on 03/04/2023).

[61] E. H. Henninger, R. C. Buschert, and Leroy Heaton. "Atomic Radial Distribution in Amorphous Selenium by X-Ray and Neutron Diffraction". en. In: *The Journal of Chemical Physics* 46.2 (Jan. 1967), pp. 586–591. ISSN: 0021-9606, 1089-7690. DOI: 10.1063/1.1840706. URL: http://aip.scitation.org/doi/10.1063/1.1840706 (visited on 10/23/2021).

[62] Wendo Wei, B.W. Corb, and B.L. Averbach. "A correlation model of amorphous selenium". en. In: *Journal of Non-Crystalline Solids* 53.1-2 (Dec. 1982), pp. 19–28. ISSN: 00223093. DOI: 10.1016/0022-3093(82)90015-1. URL: https://linkinghub.elsevier.com/retrieve/pii/0022309382900151 (visited on 03/27/2023).

[63] J. C. Slater. "Atomic Radii in Crystals". In: *The Journal of Chemical Physics* 41.10 (Nov. 1964), pp. 3199–3204. DOI: 10.1063/1.1725697.

[64] Hiroyuki Ikemoto and Takafumi Miyanaga. "Extended X-Ray Absorption Fine Structure Study of Local Structure and Atomic Correlations of Tellurium Nanoparticles". en. In: *Physical Review Letters* 99.16 (Oct. 2007), p. 165503. ISSN: 0031-9007, 1079-7114. DOI: 10.1103/PhysRevLett.99.165503. URL: https://link.aps.org/doi/10.1103/PhysRevLett.99.165503 (visited on 06/27/2020).

[65] R. Böhmer and C. A. Angell. "Elastic and viscoelastic properties of amorphous selenium and identification of the phase transition between ring and chain structures". en. In: *Physical Review B* 48.9 (Sept. 1993), pp. 5857–5864. ISSN: 0163-1829, 1095-3795. DOI: 10.1103/PhysRevB.48.5857. URL: https://link.aps.org/doi/10.1103/PhysRevB.48.5857 (visited on 09/28/2021).

[66] G. C. Das and M. B. Bever. "A thermodynamic investigation of crystalline and amorphous Se-Te alloys". en. In: *Metallurgical and Materials Transactions B* 4.6 (June 1973), pp. 1457–1461. ISSN: 1073-5615. DOI: 10.1007/BF02667994. URL: https://link.springer.com/10.1007/BF02667994 (visited on 03/27/2023).

[67] A. H. Goldan et al. "Molecular structure of vapor-deposited amorphous selenium". en. In: *Journal of Applied Physics* 120.13 (Oct. 2016), p. 135101. ISSN: 0021-8979, 1089-7550. DOI: 10.1063/1.4962315. URL: http://aip.scitation.org/doi/10.1063/1.4962315 (visited on 03/31/2021).

[68] Hiroshi Sakai. "Mossbauer Studies on the Tellurium-Selenium Mixed Chains". In: *Journal of the Phsical Society in Japan* 57.10 (Oct. 1988), pp. 3587–3593.

[69] Jingkai Qin et al. "Controlled Growth of a Large-Size 2D Selenium Nanosheet and Its Electronic and Optoelectronic Applications". en. In: *ACS Nano* 11.10 (Oct. 2017), pp. 10222–10229. ISSN: 1936-0851, 1936-086X. DOI: 10.1021/acsnano.7b04786. URL: https://pubs.acs.org/doi/10.1021/acsnano.7b04786 (visited on 06/28/2020).

[70] Seho Yi et al. "The Nature of Bonding in Bulk Tellurium Composed of One-Dimensional Helical Chains". en. In: *Inorganic Chemistry* 57.9 (May 2018), pp. 5083–5088. ISSN: 0020-1669, 1520-510X. DOI: 10.1021/acs.inorgchem.7b03244. URL: https://pubs.acs.org/doi/10.1021/acs.inorgchem.7b03244 (visited on 06/28/2020).

[71] Bengisu Sari et al. "Analysis of Strain and Defects in Tellurium-$WSe_2$ Moiré Heterostructures Using Scanning Nanodiffraction". en. In: *ACS Nano* (Nov. 2023), acsnano.3c04283. ISSN: 1936-0851, 1936-086X. DOI: 10.1021/acsnano.3c04283. URL: https://pubs.acs.org/doi/10.1021/acsnano.3c04283 (visited on 11/14/2023).

[72] Ganesh R. Bhimanapati et al. "Recent Advances in Two-Dimensional Materials beyond Graphene". en. In: *ACS Nano* 9.12 (Dec. 2015), pp. 11509–11539. ISSN: 1936-0851, 1936-086X. DOI: 10.1021/acsnano.5b05556. URL: https://pubs.acs.org/doi/10.1021/acsnano.5b05556 (visited on 12/01/2022).

[73] Karim Khan et al. "Novel Two-Dimensional Carbon–Chromium Nitride-Based Composite as an Electrocatalyst for Oxygen Reduction Reaction". en. In: *Frontiers in Chemistry* 7 (Nov. 2019), p. 738. ISSN: 2296-2646. DOI: 10.3389/fchem.2019.00738. URL: https://www.frontiersin.org/article/10.3389/fchem.2019.00738/full (visited on 11/30/2022).

[74] Adam Bolotsky et al. "Two-Dimensional Materials in Biosensing and Healthcare: From *In Vitro* Diagnostics to Optogenetics and Beyond". en. In: *ACS Nano* 13.9 (Sept. 2019), pp. 9781–9810. ISSN: 1936-0851, 1936-086X. DOI: 10.1021/acsnano.9b03632. URL: https://pubs.acs.org/doi/10.1021/acsnano.9b03632 (visited on 12/01/2022).

[75] Karim Khan et al. "Recent advances in two-dimensional materials and their nanocomposites in sustainable energy conversion applications". en. In: *Nanoscale* 11.45 (2019), pp. 21622–21678. ISSN: 2040-3364, 2040-3372. DOI: 10.1039/C9NR05919A. URL: http://xlink.rsc.org/?DOI=C9NR05919A (visited on 12/01/2022).

[76] Sanjay K. Behura et al. "Moiré physics in twisted van der Waals heterostructures of 2D materials". en. In: *Emergent Materials* 4.4 (Aug. 2021), pp. 813–826. ISSN: 2522-5731, 2522-574X. DOI: 10.1007/s42247-021-00270-x. URL: https://link.springer.com/10.1007/s42247-021-00270-x (visited on 10/20/2022).

[77] Rebeca Ribeiro-Palau et al. "Twistable electronics with dynamically rotatable heterostructures". en. In: *Science* 361.6403 (Aug. 2018), pp. 690–693. ISSN: 0036-8075, 1095-9203. DOI: 10.1126/science.aat6981. URL: https://www.science.org/doi/10.1126/science.aat6981 (visited on 10/20/2022).

[78] Yimo Han et al. "Strain Mapping of Two-Dimensional Heterostructures with Subpicometer Precision". en. In: *Nano Letters* 18.6 (June 2018), pp. 3746–3751. ISSN: 1530-6984, 1530-6992. DOI: 10.1021/acs.nanolett.8b00952. URL: https://pubs.acs.org/doi/10.1021/acs.nanolett.8b00952 (visited on 08/26/2022).

[79] Pascal Pochet et al. "Toward Moiré engineering in 2D materials via dislocation theory". en. In: *Applied Materials Today* 9 (Dec. 2017), pp. 240–250. ISSN: 23529407. DOI: 10.1016/j.apmt.2017.07.007. URL: https://linkinghub.elsevier.com/retrieve/pii/S2352940717302305 (visited on 10/19/2022).

[80] Tobias A. de Jong et al. "Imaging moiré deformation and dynamics in twisted bilayer graphene". en. In: *Nature Communications* 13.1 (Dec. 2022), p. 70. ISSN: 2041-1723. DOI: 10.1038/s41467-021-27646-1. URL: https://www.nature.com/articles/s41467-021-27646-1 (visited on 10/22/2022).

[81] Yuanyue Liu, Wenzhuo Wu, and William A. Goddard. "Tellurium: Fast Electrical and Atomic Transport along the Weak Interaction Direction". en. In: *Journal of the American Chemical Society* 140.2 (Jan. 2018), pp. 550–553. ISSN: 0002-7863, 1520-5126. DOI: 10.1021/jacs.7b09964. URL: https://pubs.acs.org/doi/10.1021/jacs.7b09964 (visited on 07/01/2020).

[82] Wenzhuo Wu et al. "Tellurene: its physical properties, scalable nanomanufacturing, and device applications". en. In: *Chemical Society Reviews* 47.19 (2018), pp. 7203–7212. ISSN: 0306-0012, 1460-4744. DOI: 10.1039/C8CS00598B. URL: http://xlink.rsc.org/?DOI=C8CS00598B (visited on 10/25/2021).

[83] Prashant Bhaskar et al. "Charge Mobility and Recombination Mechanisms in Tellurium van der Waals Solid". en. In: *The Journal of Physical Chemistry C* 123.1 (Jan. 2019), pp. 841–847. ISSN: 1932-7447, 1932-7455. DOI: 10.1021/acs.jpcc.8b09665. URL: https://pubs.acs.org/doi/10.1021/acs.jpcc.8b09665 (visited on 09/30/2020).

[84] Siqi Lin et al. "Tellurium as a high-performance elemental thermoelectric". en. In: *Nature Communications* 7.1 (Apr. 2016), p. 10287. ISSN: 2041-1723. DOI: 10.1038/ncomms10287. URL: http://www.nature.com/articles/ncomms10287 (visited on 11/04/2020).

[85] Sijia Ran et al. "Mechanical Properties and Piezoresistivity of Tellurium Nanowires". en. In: *The Journal of Physical Chemistry C* 123.36 (Sept. 2019), pp. 22578–22585. ISSN: 1932-7447, 1932-7455. DOI: 10.1021/acs.jpcc.9b05597. URL: https://pubs.acs.org/doi/10.1021/acs.jpcc.9b05597 (visited on 12/12/2022).

[86] Guolin Hao et al. "Van der waals epitaxial growth of mixed-dimensional 1D/2D heterostructures with tellurium nanowires and transition metal dichalcogenide nanosheets for nonlinear optical applications". en. In: *Materials Today Physics* 34 (May 2023), p. 101069. ISSN: 25425293. DOI: 10.1016/j.mtphys.2023.101069. URL: https://linkinghub.elsevier.com/retrieve/pii/S2542529323001050 (visited on 08/23/2023).

[87] Tatiana Latychevskaia et al. “Convergent beam electron holography for analysis of van der Waals heterostructures”. en. In: *Proceedings of the National Academy of Sciences* 115.29 (July 2018), pp. 7473–7478. ISSN: 0027-8424, 1091-6490. DOI: 10.1073/pnas.1722523115. URL: https://pnas.org/doi/full/10.1073/pnas.1722523115 (visited on 10/20/2022).

[88] Jing-Jing Xian et al. “Heterostructures of tellurium on NbSe $_2$ from sub-monolayer to few-layer films”. en. In: *Nanoscale* 12.3 (2020), pp. 1994–2001. ISSN: 2040-3364, 2040-3372. DOI: 10.1039/C9NR09445H. URL: http://xlink.rsc.org/?DOI=C9NR09445H (visited on 08/19/2021).

[89] Leo J. McGilly et al. “Visualization of moiré superlattices”. en. In: *Nature Nanotechnology* 15.7 (July 2020), pp. 580–584. ISSN: 1748-3387, 1748-3395. DOI: 10.1038/s41565-020-0708-3. URL: http://www.nature.com/articles/s41565-020-0708-3 (visited on 10/20/2022).

[90] Kate Reidy et al. “Direct imaging and electronic structure modulation of moiré superlattices at the 2D/3D interface”. en. In: *Nature Communications* 12.1 (Dec. 2021), p. 1290. ISSN: 2041-1723. DOI: 10.1038/s41467-021-21363-5. URL: http://www.nature.com/articles/s41467-021-21363-5 (visited on 05/05/2021).

[91] Jacob Madsen and Toma Susi. “The abTEM code: transmission electron microscopy from first principles”. en. In: *Open Research Europe* 1 (Mar. 2021), p. 24. ISSN: 2732-5121. DOI: 10.12688/openreseurope.13015.1. URL: https://open-research-europe.ec.europa.eu/articles/1-24/v1 (visited on 12/16/2022).

[92] C. Adenis, V. Langer, and O. Lindqvist. “Reinvestigation of the structure of tellurium”. en. In: *Acta Crystallographica Section C Crystal Structure Communications* 45.6 (June 1989), pp. 941–942. ISSN: 01082701. DOI: 10.1107/S0108270188014453. URL: https://scripts.iucr.org/cgi-bin/paper?S0108270188014453 (visited on 12/21/2022).

[93] M. Schlüter et al. “The structural nature of amorphous Se and Te”. en. In: *Solid State Communications* 15.6 (Sept. 1974), pp. 1007–1010. ISSN: 00381098. DOI: 10.1016/0038-1098(74)90519-5. URL: https://linkinghub.elsevier.com/retrieve/pii/0038109874905195 (visited on 06/28/2020).

[94] Peter Ercius et al. “The 4D Camera – An 87 kHz Frame-rate Detector for Counted 4D-STEM Experiments”. en. In: *Microscopy and Microanalysis* 26.S2 (Aug. 2020), pp. 1896–1897. ISSN: 1431-9276, 1435-8115. DOI: 10.1017/S1431927620019753. URL: https://www.cambridge.org/core/product/identifier/S1431927620019753/type/journal_article (visited on 01/31/2023).

[95] Steven E. Zeltmann et al. “Patterned Probes for High Precision 4D-STEM Bragg Measurements”. en. In: *Ultramicroscopy* 209 (Feb. 2020). arXiv: 1907.05504, p. 112890. ISSN: 03043991. DOI: 10.1016/j.ultramic.2019.112890. URL: http://arxiv.org/abs/1907.05504 (visited on 03/30/2022).

[96] E.J. Weidman and J.C. Anderson. “Structure and growth of oriented tellurium thin films”. In: *Thin Solid Films* (Oct. 1970).

[97] G. S. Bales and A. Zangwill. “Morphological instability of a terrace edge during step-flow growth”. en. In: *Physical Review B* 41.9 (Mar. 1990), pp. 5500–5508. ISSN: 0163-1829, 1095-3795. DOI: 10.1103/PhysRevB.41.5500. URL: https://link.aps.org/doi/10.1103/PhysRevB.41.5500 (visited on 12/23/2022).

[98] Anubhav Jain et al. “Commentary: The Materials Project: A materials genome approach to accelerating materials innovation”. en. In: *APL Materials* 1.1 (July 2013), p. 011002. ISSN: 2166-532X. DOI: 10.1063/1.4812323. URL: http://aip.scitation.org/doi/10.1063/1.4812323 (visited on 10/13/2022).

[99] Wenyang Ding et al. “Mechanical responses of WSe $_2$ monolayers: a molecular dynamics study”. en. In: *Materials Research Express* 6.8 (May 2019), p. 085071. ISSN: 2053-1591. DOI: 10.1088/2053-1591/ab2085. URL: https://iopscience.iop.org/article/10.1088/2053-1591/ab2085 (visited on 08/23/2023).

[100] J. C. Doukhan et al. “Observation of Dislocations in Tellurium by Transmission Electron Microscopy”. en. In: *physica status solidi (b)* 35.2 (1969), pp. 835–842. ISSN: 03701972, 15213951. DOI: 10.1002/pssb.19690350233. URL: https://onlinelibrary.wiley.com/doi/10.1002/pssb.19690350233 (visited on 06/21/2022).

[101] J. P. Estienne and J. L. Farvacque. “Occurrence of an “” screw dislocation substructure in tellurium by a torsion experiment”. en. In: *Physica Status Solidi (a)* 49.2 (Oct. 1978), K109–K111. ISSN: 00318965, 1521396X. DOI: 10.1002/pssa.2210490250. URL: https://onlinelibrary.wiley.com/doi/10.1002/pssa.2210490250.

[102] Zhuofa Chen et al. “Charge Separation in Monolayer WSe $_2$ by Strain Engineering: Implications for Strain-Induced Diode Action”. en. In: *ACS Applied Nano Materials* 5.10 (Oct. 2022), pp. 15095–15101. ISSN: 2574-0970, 2574-0970. DOI: 10.1021/acsanm.2c03264. URL: https://pubs.acs.org/doi/10.1021/acsanm.2c03264 (visited on 05/10/2023).

[103] Luis A. Agapito et al. “Novel Family of Chiral-Based Topological Insulators: Elemental Tellurium under Strain”. en. In: *Physical Review Letters* 110.17 (Apr. 2013), p. 176401. ISSN: 0031-9007, 1079-7114. DOI: 10.1103/PhysRevLett.110.176401. URL: https://link.aps.org/doi/10.1103/PhysRevLett.110.176401 (visited on 05/10/2023).

[104] Joshua Pelleg. *Mechanical Properties of Materials*. en. Vol. 190. Solid Mechanics and Its Applications. Dordrecht: Springer Netherlands, 2013. ISBN: 978-94-007-4341-0 978-94-007-4342-7. DOI: 10.1007/978-94-007-4342-7. URL: https://link.springer.com/10.1007/978-94-007-4342-7 (visited on 10/23/2023).

[105] David Roylance. “STRESS-STRAIN CURVES”. en. In: ().

[106] Chao Cai and Kun Zhou. “Metal additive manufacturing”. en. In: *Digital Manufacturing*. Elsevier, 2022, pp. 247–298. ISBN: 978-0-323-95062-6. DOI: 10.1016/B978-0-323-95062-6.00005-X. URL: https://linkinghub.elsevier.com/retrieve/pii/B978032395062600005X (visited on 10/24/2023).

[107] M Nabil Bassim and C D Liu. “Dislocation cell structures in copper in torsion and tension”. en. In: ().

[108] Z. W. Shan et al. “Mechanical annealing and source-limited deformation in submicrometre-diameter Ni crystals”. en. In: *Nature Materials* 7.2 (Feb. 2008), pp. 115–119. ISSN: 1476-1122, 1476-4660. DOI: 10.1038/nmat2085. (Visited on 10/24/2023).

[109] Rafael Roldán et al. “Strain engineering in semiconducting two-dimensional crystals”. en. In: *Journal of Physics: Condensed Matter* 27.31 (Aug. 2015), p. 313201. ISSN: 0953-8984, 1361-648X. DOI: 10.1088/0953-8984/27/31/313201. URL: https://iopscience.iop.org/article/10.1088/0953-8984/27/31/313201 (visited on 11/16/2023).

[110] Zhuoya Dong and Yanhang Ma. “Atomic-level handedness determination of chiral crystals using aberration-corrected scanning transmission electron microscopy”. en. In: *Nature Communications* 11.1 (Dec. 2020), p. 1588. ISSN: 2041-1723. DOI: 10.1038/s41467-020-15388-5. URL: http://www.nature.com/articles/s41467-020-15388-5 (visited on 07/29/2020).

[111] Siegfried Schmauder et al., eds. *Handbook of Mechanics of Materials*. en. Singapore: Springer Singapore, 2019. ISBN: 978-981-10-6883-6 978-981-10-6884-3. DOI: 10.1007/978-981-10-6884-3. URL: http://link.springer.com/10.1007/978-981-10-6884-3 (visited on 10/24/2023).

[112] Fang Liu et al. “Disassembling 2D van der Waals crystals into macroscopic monolayers and reassembling into artificial lattices”. en. In: *Science* 367.6480 (Feb. 2020), pp. 903–906. ISSN: 0036-8075, 1095-9203. DOI: 10.1126/science.aba1416. URL: https://www.science.org/doi/10.1126/science.aba1416 (visited on 10/19/2023).

[113] Ying Han et al. “Deep Elastic Strain Engineering of 2D Materials and Their Twisted Bilayers”. en. In: *ACS Applied Materials & Interfaces* 14.7 (Feb. 2022), pp. 8655–8663. ISSN: 1944-8244, 1944-8252. DOI: 10.1021/acsami.1c23431. URL: https://pubs.acs.org/doi/10.1021/acsami.1c23431 (visited on 10/26/2023).

[114] Huixia Yang et al. “Moiré Pattern Dislocation in Continuous Atomic Lattice of Monolayer h-BN”. en. In: *ACS Applied Electronic Materials* 4.2 (Feb. 2022), pp. 891–896. ISSN: 2637-6113, 2637-6113. DOI: 10.1021/acsaelm.2c00013. URL: https://pubs.acs.org/doi/10.1021/acsaelm.2c00013 (visited on 10/12/2022).

[115] Sandhya Susarla et al. “Mapping Modified Electronic Levels in the Moiré Patterns in $MoS_2$/$WSe_2$ Using Low-Loss EELS”. en. In: *Nano Letters* 21.9 (May 2021), pp. 4071–4077. ISSN: 1530-6984, 1530-6992. DOI: 10.1021/acs.nanolett.1c00984. URL: https://pubs.acs.org/doi/10.1021/acs.nanolett.1c00984 (visited on 11/02/2023).